

Department of Physics and Astronomy

University of Heidelberg

Diploma thesis

in Physics

submitted by

Arno John

born in Heidelberg (Germany)

2011



**Data Reduction at Front End Level**  
**in a Level-1 Track Trigger**  
**for the ATLAS High-Luminosity Upgrade**

This diploma thesis has been carried out by Arno John

at the

Physikalisches Institut der Universität Heidelberg

under the supervision of

Prof. Dr. André Schöning



# Abstract

Long term plannings for the Large Hadron Collider foresee an upgrade by the year 2020, with the aim to increase the luminosity by an order of magnitude to  $L = 10^{35} \text{cm}^{-2} \text{s}^{-1}$ , allowing to analyse rare events on a improved statistical basis.

A luminosity upgrade implies challenging adaptations of the LHC experiments. The detector occupancies as well as the amount of data to be read out from the front end systems will greatly increase, while e.g. at ATLAS, the amount of permanently stored data per bunch crossing is required to stay at the current level. The improvement of the trigger system is one of the main approaches to tackle these increased demands. It is planned to implement track reconstruction already at the first, hardware based, trigger level.

Due to bandwidth limitations at the front end system, data reduction before read-out is required for a track trigger implemented in hardware. A data reduction at front end level can be achieved by selecting hits associated with high momentum particles, which are relevant for triggering physics processes at the electroweak scale or higher. In this thesis, two methods which allow a selection of high transverse momentum hits in the inner detector of ATLAS before track reconstruction are presented and analysed.

# Zusammenfassung

Langfristige Planungen für den Large Hadron Collider sehen für 2020 ein Upgrade vor, mit dem Ziel die Luminosität um eine Grössenordnung auf  $L = 10^{35} \text{cm}^{-2} \text{s}^{-1}$  zu erhöhen, um die Untersuchung seltener Ereignisse auf einer verbesserten statistischen Grundlage zu ermöglichen.

Die erhöhte Luminosität stellt für die Experimente am LHC eine große Herausforderung dar. Trotz erhöhter Detektorokkupanz und der gesteigerter Menge Daten, welche am Frontend ausgelesen werden müssen, soll z.B. bei ATLAS die Menge der permanent gespeicherten Daten pro bunch crossing auf dem heutigen Stand bleiben. Eine Verbesserung des Triggersystems ist einer der wichtigsten Ansätze um den gesteigerten Ansprüchen gerecht zu werden. Es ist geplant eine Spurrekonstruktion bereits in der ersten Triggerstufe, welche komplett in Hardware implementiert ist, einzuführen.

Aufgrund der limitierten Bandbreite am Frontend System ist eine Reduktion der Daten vor dem Auslesen nötig, um einen in Hardware realisierten Spurtrigger zu ermöglichen. Eine Datenreduktion auf Frontend Stufe kann durch eine Vorauswahl von Treffern, welche von Teilchen mit hohem Impuls stammen und daher für das Triggern von Prozessen auf der elektroschwachen und höheren Skalen relevant sind, erreicht werden. In dieser Diplomarbeit werden zwei Methoden vorgestellt und analysiert, welche eine Auswahl von Treffern mit hohem Transversalimpuls im inneren Detektor von ATLAS schon vor der Spurrekonstruktion ermöglichen.



# Contents

<b>1</b>	<b>Motivation</b>	<b>9</b>
<b>2</b>	<b>Introduction</b>	<b>11</b>
2.1	The Large Hadron Collider (LHC) . . . . .	11
2.2	The ATLAS Experiment . . . . .	13
2.3	The High Luminosity Upgrade for LHC and ATLAS . . . . .	19
2.4	Geometry of the Upgraded Silicon Strip Detector . . . . .	23
2.5	Transverse Momentum Determination at Module Level . . . . .	26
<b>3</b>	<b>Upgrade Detector Simulation</b>	<b>29</b>
3.1	Detector Simulation Software . . . . .	29
3.2	Data Samples . . . . .	29
<b>4</b>	<b>Offset and Cluster Size Dependences</b>	<b>37</b>
4.1	Transverse Momentum and Charge Dependence . . . . .	37
4.2	Dependence on Module Impact Point . . . . .	40
4.3	Cluster Size Decomposition . . . . .	44
<b>5</b>	<b>Offset Cut Implementation</b>	<b>47</b>
5.1	Theoretical Calculation of Coincidence Offsets . . . . .	47
5.2	Validation Region . . . . .	51
<b>6</b>	<b>Data Reduction Rates</b>	<b>57</b>
6.1	Reduction Rate with Single Muon Events . . . . .	57
6.2	Hit Rejection Rate with Single Pion and Electron Events . . . . .	60
6.3	Combined Application of Cluster Size and Offset Cut . . . . .	61
6.4	Reduction Rate Estimation with Minimum Bias Events. . . . .	62
6.5	Track Reconstruction . . . . .	64
<b>7</b>	<b>Summary</b>	<b>69</b>
<b>A</b>	<b>Appendix</b>	<b>71</b>
A.1	Luminosity . . . . .	71
A.2	The ATLAS Coordinate System . . . . .	72
A.3	The Detector Simulation Data Format . . . . .	72
A.4	Code Implementation of the Hit Validation . . . . .	73
A.5	List of Figures . . . . .	74
A.6	List of Tables . . . . .	77



# 1 Motivation

The Standard Model of particle physics has proven to be a very valuable theory by correctly predicting an overwhelming amount of the results of experiments performed in the last decades. However, it fails to provide explanations for fundamental questions. For example, the Standard Model is unable to predict masses of elementary particles. Other important issues are the matter/antimatter asymmetry in the universe, the existence of dark matter and the missing explanations for the existence of the three generations of leptons and quarks that have been found so far.

The Large Hadron Collider, located at the CERN in Geneva, is currently the world's largest project addressing these fundamental questions of particle physics. The LHC aims to confirm or disprove the existence of the Higgs particle, as well as numerous theories beyond the Standard Model, with the Supersymmetry being the most popular.

First runs at the LHC were made in 2008, and after a breakdown followed by more than one year of maintenance, regular data taking started in late 2009. Already before completion, plannings for an upgrade for the LHC started, with the objective to increase the instantaneous luminosity by an order of magnitude. The increased luminosity will allow the studies of rare events based on improved statistics.

A luminosity upgrade requires not only changes in the particle accelerator itself. The collider experiments need to be adapted to the more challenging environment: a higher luminosity signifies an enhanced particle production, therefore an increased amount of information needs to be read out and processed. This implies adaptations of the components, the designs and the trigger systems of the detectors.

For the ATLAS experiment, introduced in chapter 2, it is planned to improve the performance of the trigger system by introducing a track trigger at the first, hardware based level. To comply latency constraints, track triggering needs to be implemented by fast pattern matching. Currently, track reconstruction is done by software from trigger level 2 onwards.

In order to perform pattern matching at a high detector occupancy and with limited read out bandwidth, a preselection of hits originating from particles with a high transverse momentum is required. The standard way to determine the transverse momentum of a particle is to measure the bending radius of the track in the magnetic field of the detector. This is obviously not possible before track reconstruction has taken place. For the hit preselection one therefore has to exploit other properties, that are based on track deflection in the magnetic field as well, but which can be determined within the small scaled front-end systems before the read out of detector modules.

In the silicon strip detector of ATLAS, two measurement parameters can be used

for such a hit preselection. One is based on the property of low momentum particles to form clusters of isolated hits, the other exploits the double layer structure of silicon strip modules by measuring the offset between the hits on the front and back side.

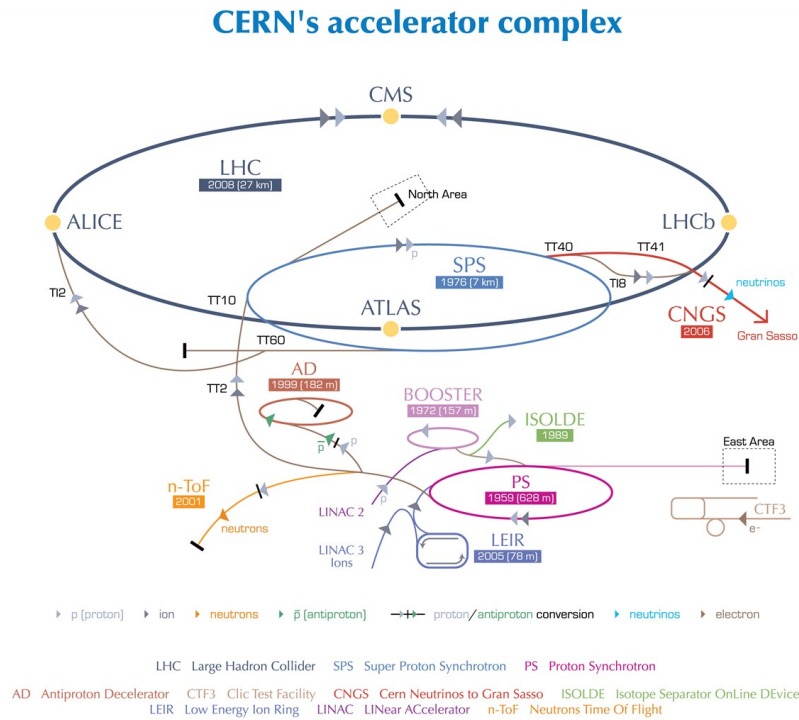
For this thesis, studies based on an ATLAS upgrade detector simulation were performed in order to investigate the above-mentioned methods for hit filtering. The simulation software and therewith produced simulation data are described in chapter 3. In chapter 4, the dependence of the hit cluster size and the offset of double layer coincidences on the transverse momentum is determined. Further parameters, e.g. the dependence on the hit position and the particle charge are analysed. The implementation of an offset based hit selection is discussed in chapter 5. The performance of the hit selections is determined in chapter 6. A summary is given in Chapter 7.

## 2 Introduction

### 2.1 The Large Hadron Collider (LHC)

The LHC is the world's largest particle accelerator, located at the European Organization for Nuclear Research (CERN) in Geneva, Switzerland. It is a synchrotron and storage ring with a circumference of 27 km, designed for proton-proton collisions with a center of mass energy of up to  $\sqrt{s} = 14$  TeV at an instantaneous luminosity<sup>1</sup> of  $L = 10^{34} \text{cm}^{-2}\text{s}^{-1}$ . Aside pp-collisions, the rings can also be filled with lead nuclei with a center mass energy of  $\sqrt{s} = 5.5$  TeV and  $L = 10^{27} \text{cm}^{-2}\text{s}^{-1}$ .

Although the official first run at LHC was on September 10th 2008, regular data taking did not start until 2010 after a breakdown due to technical issues. The LHC currently runs at 3.5 TeV per beam, the designated center of mass energy will not be reached before 2014.



European Organization for Nuclear Research | Organisation européenne pour la recherche nucléaire

© CERN 2008

**Figure 2.1:** CERN - Overview of the CERN accelerator complex [9].

<sup>1</sup>see Appendix A.1

## The LHC Accelerator Chain

Free protons are obtained by ionising hydrogen atoms. The protons are firstly accelerated by the linear accelerator Linac 2 to an energy of 50 MeV. After being further preaccelerated by the Proton Synchrotron Booster (PSB, 1.4 GeV), the Proton Synchrotron (PS, 26 GeV) and the Super Proton Synchrotron (SPS, 450 GeV), the protons are injected into the LHC ring where they finally attain their peak energy of 7 TeV (fig. 2.1).

The protons are accumulated in *bunches* containing up to  $10^{11}$  protons each. Both beams get filled with at most 1404 bunches (in may 2011: 874 bunches[4]), resulting in a maximum of 40 million bunch crossings per second at the interaction points.

## Objectives of the LHC

Providing a center of mass energy significantly higher than ever reached before in particle accelerators, the goals of LHC are not only verification of results of previous experiments but the search for new physics at the terascale. In particular, the discovery of hypothetical particles like the Higgs-Boson and light particles predicted by supersymmetry are often stated as the main objectives of LHC.

- The **Higgs-Mechanism** is a theory explaining the origin of the mass of elementary particles within the Standard Model. It requires the existence of the Higgs-Boson, the last particle of the Standard Model that has not been discovered yet.

The mass scale, in which the Higgs-Boson is to be found, has been confined by previous experiments, theory and statistical considerations: The forerunners of LHC, the LEP and Tevatron excluded a Higgs mass of below  $114 \text{ GeV}/c^2$  and the interval  $160$  to  $170 \text{ GeV}/c^2$  respectively, indirect constrains foresees the mass to be most likely below  $185 \text{ GeV}/c^2$ . As the remaining energy region will be covered by the LHC, the Higgs-Boson will be detected in case it exists according to established theories.

- The theory of **Supersymmetry** assigns to every particle in the Standard Model another particle, called super-partner, with identical quantum numbers except the spin. Superpartners have a spin differing by  $1/2$ , causing superpartners of fermions to be bosons and vice versa.

Although there are no experimental evidences, supersymmetric theories are very popular because of their potential to solve fundamental problems of modern physics like the explanation of dark matter and the unification of electroweak and strong interaction at high energies.

At the Tevatron, masses for the lightest supersymmetric particles below  $300 \text{ GeV}/c^2$  have been excluded. As theory does not predict an upper mass boundary for superpartners, LHC might not be able to bring as decisive perceptions for Supersymmetry as for the Higgs-Mechanism.

Beside the search for new particles, the LHC will allow measurements at higher precision compared to previous experiments, for example:

- With a **top quark** production cross section significantly higher than ever before, the LHC will allow greatly improved mass measurements of the top quark as well as heavy bosons.
- Improved measurements of the **CKM-matrix** via measurements with b-quarks. The CKM-matrix describes CP violation of the weak interaction..
- Lead-lead collisions allow the studying of the **Quark-gluon plasma**, a phase of matter at the very early stages of the universe.

## 2.2 The ATLAS Experiment

The ATLAS detector (fig. 2.2) is one of the four main detector experiments at the LHC with a length of 44 m and a diameter of 25 m, weighing approximately 7,000t. Being one of the two general purpose detectors of the LHC, its role is to collect as much information as possible from the decay products of particles produced at proton-proton collisions in order to search for new physics. Because of the high luminosity and high energy at the LHC, the detector needs to satisfy several demanding requirements: fast particle detection and data read-out electronics, radiation hard components, high sensor granularity and tracking resolution as well as a sophisticated trigger system.

ATLAS consists of three subdetectors, with increasing distance from the interaction point: the inner detector, the calorimeter system and the muon spectrometer, as well as two magnet systems. The basic geometry is the same for all subdetectors: a barrel around the beam axis for full coverage in  $\phi$  (azimuth angle) and end-caps at each end for increased pseudorapidity  $\eta$  acceptance (see Appendix A.2: The ATLAS Coordinate System).

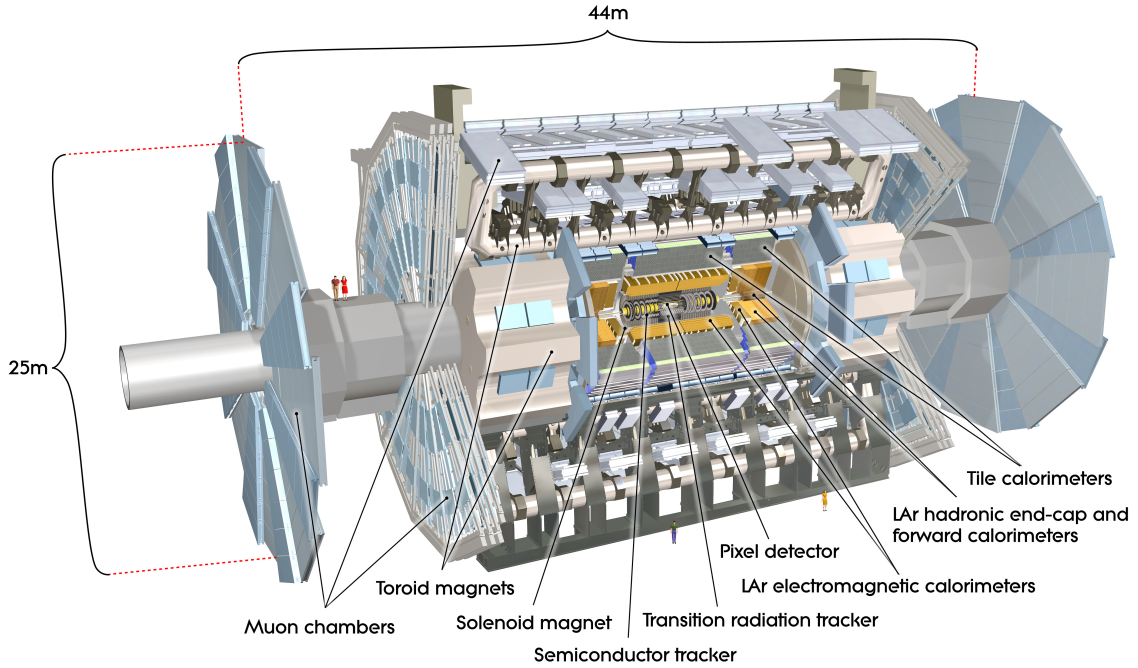


Figure 2.2: The ATLAS experiment - cut-away view [6].

## Magnet Systems

The ATLAS magnet system generates two magnetic fields. Surrounding the inner detector, a solenoid shaped superconductive magnet provides a constant magnetic field in beam direction of  $B = 2$  T, strong enough to bend even very high energetic particles sufficiently to determine their transverse momentum in the inner detector. In the muon system, a toroidal magnetic field of approximately  $B = 0.5$  T is produced by eight large superconductive coils and two toroids in the end-caps. The direction of the resulting magnetic field is about orthogonal to the particles trajectory.

## Inner Detector

The purpose of the inner detector (fig. 2.3) is the tracking of charged particles. It is divided in three independent subdetectors, all of them together covering the pseudorapidity range  $|\eta| < 2.5$ .

- **Pixel Detector:** located closest to the interaction point, the pixel detector uses silicon technology and provides the highest tracking resolution of the inner detector. In particular, it collects valuable data for track origin (vertex) extrapolation. The Pixel detector has three layers consisting of a total of 1744 modules with each 47,232 pixels of  $50 \mu\text{m} \times 400 \mu\text{m}$  size, and a total of 140 million channels.

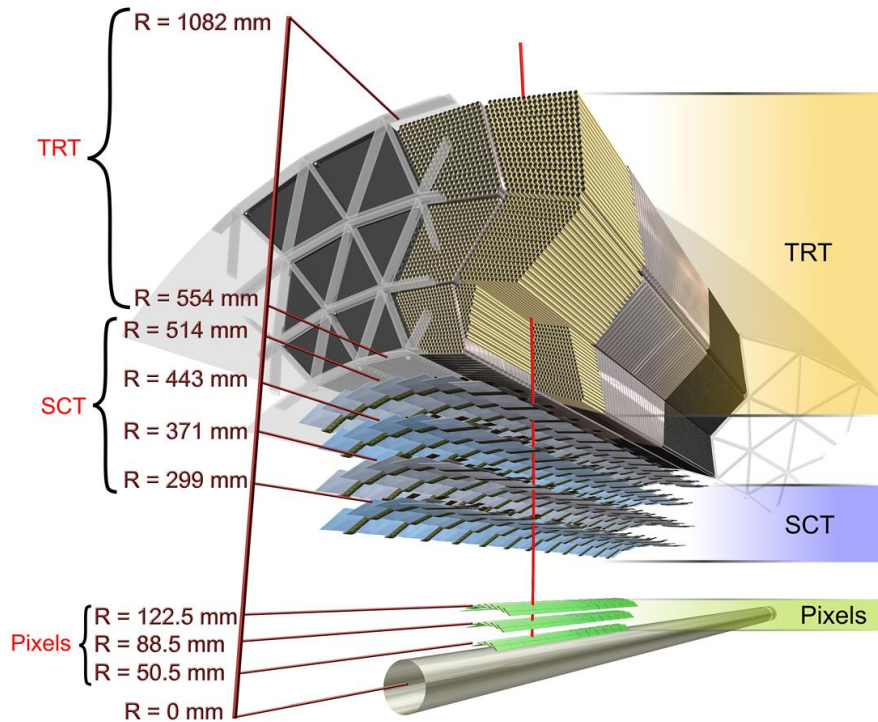


**Figure 2.3:** The ATLAS Inner Detector - figure showing the three subdetectors [6].

- Semi Conductor Tracker (SCT):** The middle part of the inner detector has 4 double-sided layers with a total 15,912 modules composed of 768 strips of  $80\ \mu\text{m}$  pitch, with 6.2 million channels. Despite having a worse granularity than the pixel detector, the SCT provides essential informations for track reconstruction by measuring more hits over a larger area.
- Transition Radiation Tracker (TRT):** The main purpose of this straw detector is the measuring of transition radiation, which allows to differentiate between electrons and pions. In addition, the TRT contributes to track reconstruction with an average of 36 hits per track with  $200\ \mu\text{m}$ -precision, provided by approximately 300.000 straw tubes and 420.000 channels.

The detailed tracking information collected by the inner detector permits to determine the charge of particles as well as to calculate the transverse momentum from the curvature of the track.

Because of the proximity to the interaction point, the inner detector is in a high-radiation environment, requiring the usage of radiation hardened components. It

is expected that the inner detector will need to be replaced after a running time corresponding to an integrated luminosity of  $300 \text{ fb}^{-1}$ .

## Calorimeters

The purpose of calorimeters (fig. 2.4) is to measure the energy of particles. There are two basic calorimeter systems in the ATLAS detector, the electromagnetic and the hadronic. Both are sampling calorimeters, whose functional principle is to measure the energy by absorption in high density metals.

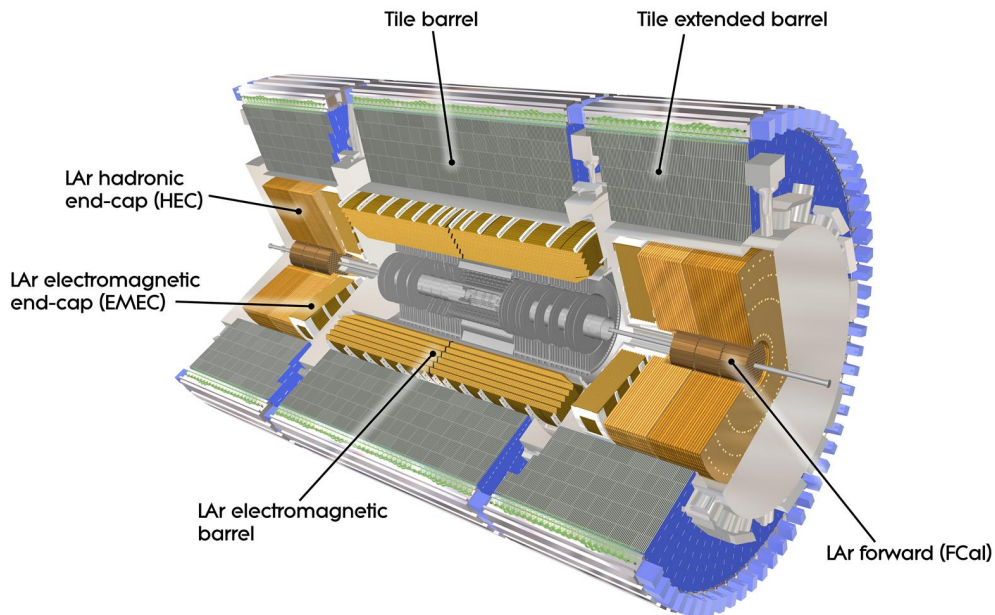


**Figure 2.4:** The ATLAS calorimeter system - cut-away view [6].

- The inner **electromagnetic calorimeter** absorbs energy from particles that interact electromagnetically. Its characteristics are high precision in energy and location. It is based on lead - liquid argon technology (LAr), with lead and steel as absorbing materials and liquid Argon as sensing element.
- The outer **hadronic calorimeter** absorbs the energy of particles that pass the electromagnetic calorimeters and interact by the strong force, in most cases hadrons. In comparison, it has a lower resolution. For this type of calorimeter, tiles of scintillating plastic are used as sensor, with steel as absorber material.

The data collected by the calorimeters is for example used to determine electron and photon energy, for jet reconstruction and the calculation of missing energy.

## Muon Spectrometer

Similar to the Inner Detector, the muon system allows the calculation of transverse momentum by measuring the bending radius of the particle in a magnetic field using tracking chambers, namely the Monitored Drift Tube chambers (MDT) and the Cathode-Strip Chambers (CSC). Being the largest part of the detector, it has a relatively low spatial precision but compensates this by measuring over a large volume area. As the muon spectrometer is located outside the calorimeters, only muons reach this part of the detector, so that the muon spectrometer can be used for muon identification as well. This is done by the trigger chambers: the Resistive Plate Chambers (RPC) and the Thin Gap Chambers (TGC).

## Trigger System

For bunch crossings every 25 ns (40 MHz) and 23 proton-proton collisions per bunch crossing, resulting in roughly 40 Terabyte of raw data per second, it is impossible to permanently save all information taken in the ATLAS detector. The trigger system reduces data output by selecting the most interesting events, up to 200 per second. It is divided into three levels, with an increasing amount of information that is used for decisions and increasing processing time (fig. 2.5).

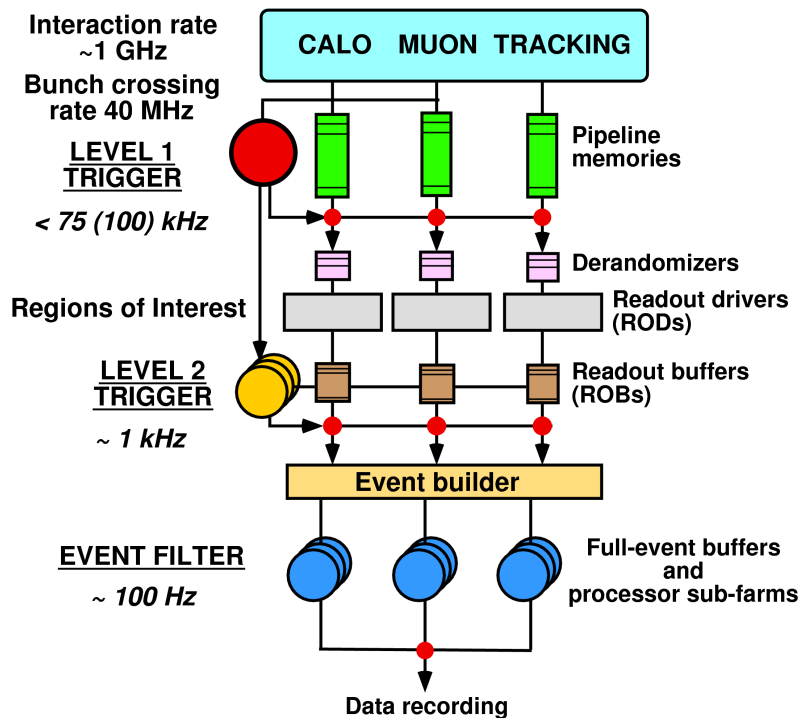


Figure 2.5: The ATLAS Trigger System - Overview [2].

- **Level 1:** the first trigger level is completely implemented in detector electronics using pipeline processors in parallel architecture and has a latency of 2.5

$\mu\text{s}$ . It uses a subset (lower granularity) of information from the calorimeter (L1Calo) and muon system (L1Muon) to look for high  $p_t$  photons, electrons, muons and tauons as well as events with high amounts of missing transverse energy or high total transverse energy. Until the trigger decision is made, the whole raw detector output needs to be stored in pipeline memories. The event rate is reduced to a maximum of 75 kHz.

- **Level 2:** the second trigger level is software based and runs on commercial computer clusters. It is seeded by Regions-of-Interest (ROI) defined by the Level 1 Trigger and uses information from all parts of the detector at full granularity. While waiting for a decision to be made, the data is temporarily stored in readout buffers. The average processing time is 40 ms and the event rate is reduced to below 3.5 kHz.
- **Event filter:** As the data of events selected by the L2 trigger are fragmented over readout buffers from all subdetectors, they need to be joined by the event builder. The event filter, as last trigger level, then runs offline analysis on processor farms over the full events, further reducing the event rate to approximately 200 Hz which corresponds to roughly 320 Megabyte per second.

The L2 trigger and event filter together form the **High-Level-Trigger** (HLT).

## Data Acquisition System (DAQ)

The data acquisition system is responsible for data transfer between trigger levels:

- Receives and buffers event data from subdetectors at L1 trigger rate.
- Transmits requested data (corresponding to ROIs) to L2 and, in case of a positive L2 trigger decision, to the event builder.
- Transmits assembled data from the event builder to the event filter and further, if selected, to permanent storage.

The Detector Control System (DCS) provides for configuration, control and monitoring during data taking.

## 2.3 The High Luminosity Upgrade for LHC and ATLAS

In order to improve sensitivity for rare events, like e.g. the Higgs-Boson decay, a luminosity upgrade by an order of magnitude for the LHC is currently in the planning and is set for 2020 at the earliest. The raised luminosity  $L = 10^{35} \text{cm}^{-2} \text{s}^{-1}$ , corresponding to up to 400 pp-collisions per bunch crossing (fig. 2.6) for a 50 ns bunch spacing, will be attained by increasing the amount of protons per bunch and a higher beam focus, using improved focussing magnets.

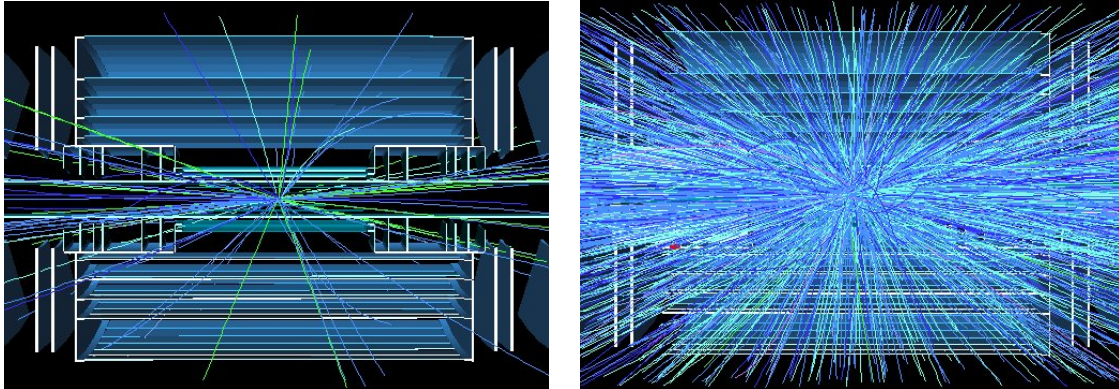


**Figure 2.6:** Two pictures of a simulation showing the tracks in the upgraded inner detector resulting from one bunch crossing, corresponding to a luminosity of  $L = 0.2 * 10^{34} \text{cm}^{-2} \text{s}^{-1}$  (left, 5 collisions) and  $L = 10.0 * 10^{34} \text{cm}^{-2} \text{s}^{-1}$  (right, 200 collisions) [1].

The LHC detectors will need to be upgraded to satisfy the increased requirements to data taking, data selection/reduction and radiation hardness caused by event pileup<sup>2</sup> and increased hit occupancy respectively. At ATLAS, the goal is to achieve a similar detector performance while keeping the amount of data recording at a reasonable level, comparable to the current setup. This will in particular require adaptations to the detector design and major improvements in the ATLAS trigger system.

For the DAQ and the trigger systems, pileup and higher detector occupancy imply challenging consequences:

- For similar  $p_t$ -thresholds, the trigger rate is expected to go up by an order of magnitude.
- Even at a Level 1 trigger rate similar to the current (75 kHz), the increased occupancy requires more readout bandwidth. The amount of data that needs to be stored at disk is expected to be 5 to 10 times larger [11].

---

<sup>2</sup>pileup: multiple proton-proton collisions per bunch crossing

- Increasing detector occupancy makes pattern recognition more difficult.

### Modifications to the Inner Detector Layout

As the planning for the ATLAS upgrade is work in progress, the final inner detector design is not yet decided. Current plans are to remove the transition radiation tracker in favor for larger Pixel and SCT detectors (fig. 2.7), along with an overall higher granularity. Table 2.1 shows a comparison of the layouts of the current and the upgraded Pixel and SCT detectors. Measuring track hits with higher granularity in a larger area will not only improve the tracking precision but also lower the occupancy in order to compensate for the increased pileup.

A consequence of these adaptations is the largely increasing amount of required channels, which brings additional challenges to the DAQ system and the Triggers. Table 2.2 shows the increase of the number of channels with the upgrade.

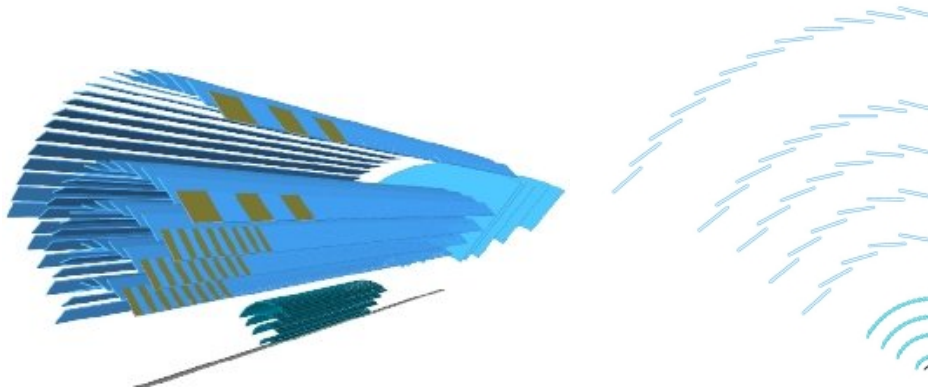


**Figure 2.7:** Inner Detector of ATLAS Upgrade: 3D view (left) and figure of the xy-plane (right), showing the four pixel layers close to the beam lines and five SCT layers [7].

### Trigger Upgrades

With increasing luminosity and consequently, increased data output to be handled, the ATLAS trigger system will require challenging improvements. This is especially important at the first trigger level. In order to reduce the trigger rate at level 1 without affecting efficiency, it is essential to provide additional information for the trigger decision.

A first approach is to enable access to full granularity from the calorimeters and muon system to the L1Calo and L1Muon triggers. However, preliminary studies have shown that, in order to maintain a trigger rate of 75 kHz, the  $p_t$ -threshold has to be raised to 60 GeV/c for single electrons and muons [13], causing significant losses of interesting electroweak-scale events.

<b>Pixel geometry</b>	<b>ATLAS</b>	<b>ATLAS Upgrade</b>
layers	3	4
radius range [mm]	50 - 122.5	37 - 200
pixel size [ $\mu\text{m}$ ]	50x400	50x250
<b>SCT geometry</b>		
layers	4	3(short) + 2(long)
radius range [mm]	299 - 514	380 - 1000
amount of modules (barrel)	2112	13,440
module width [cm]	10	10
strips per module	768	1280
strip & module length [cm]	12	2.5(short) / 10(long)

**Table 2.1:** Comparison of inner detector layouts.

<b>Channels (in million)</b>	<b>ATLAS</b>	<b>ATLAS Upgrade</b>
Pixel Detector	140	300
Silicon Strip Detector	6.2	43
Transition Radiation Tracker	0.42	-

**Table 2.2:** Number of channels in the inner detector, before and after upgrade.

Therefore, a promising project is to introduce a track trigger at level 1, which is able to recognize events containing a high transverse momentum track. This will allow lower  $p_t$ -thresholds without increasing the trigger rate. For now, track reconstruction has not been utilized for trigger decisions until level 2, which uses software based methods. A reconstruction is too slow for trigger level 1 and can not be implemented in hardware, therefore another approach is needed, as discussed in the next section. An important issue with a level 1 track trigger is the large amount of channels in the inner detector, making a full readout at a rate of 40 MHz for triggering purposes impossible. Two approaches to address this problem were proposed [11]:

- **RoI Seeding:** The RoI seeding approach uses Region of Interests defined in  $(\eta, \phi)$  by L1Calo and L1Muon to request what part of the inner detector needs to be read out. Using this method, the read out rate could be lowered from 40 MHz to  $\sim 500$  kHz. This approach would lead to an increase of the latency of trigger level 1, as the read out needs to wait for ROI information from outside the inner detector.
- **Self Seeding:** The self seeding is a standalone method that does not rely on informations from other parts of the detector. Instead, dedicated tracking layers are used to find high- $p_t$  tracks, allowing information from the full event

to be processed at 40 MHz. The result from the track trigger can later be used in combination with results from L1Calo and L1Muon.

## Fast Tracking by Pattern Matching

Track reconstruction using software based methods is not possible at Trigger Level 1 because of timing and bandwidth constraints. Instead, it is planned to apply pattern matching by comparing hit patterns from the SCT with precalculated templates of high-momentum tracks, stored in hardware look-ups.

The usage of Content Addressable Memory (CAM) allows to compare a pattern with all stored templates in very short time (fig. 2.8). A high momentum pattern only covers a relatively small area of the detector, therefore only a certain region needs to be read out.

To reduce the bandwidth requirements as well as the amount of fake matches at high detector occupancies, a filtering of hits is required before the pattern matching. Analysing methods for preselecting high- $p_t$  hits in hardware, at module level, is subject of this thesis.

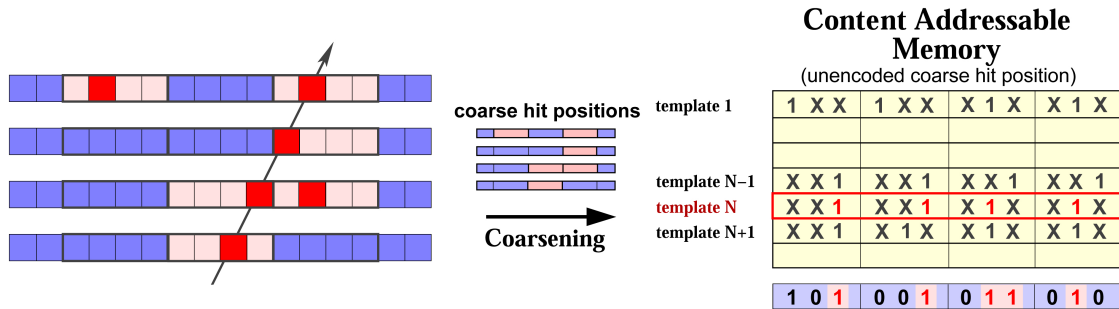


**Figure 2.8:** Implementation of the hit pattern matching using a CAM for fast look-up [13] (simplified).

A pattern is created from hits on different detector layers and quickly compared with templates of high-energy tracks using Content Addressable Memory.

## 2.4 Geometry of the Upgraded Silicon Strip Detector

The final design of the ATLAS upgrade is not decided yet. The following section describes the SCT barrel detector geometry version [7] that has been used in the simulation studies performed for this thesis.

### SCT Barrel

The SCT Barrel has 5 layers, consisting of modules aligned in rows in  $z$  direction. The modules are tilted by  $10^\circ$  from the tangential orientation in order to compensate for the lorentz angle and provide a full coverage in  $\phi$  by overlapping.

Figure 2.9 shows a 3D view of 5 layers of the upgrade SCT barrel, table 2.3 contains geometry details.

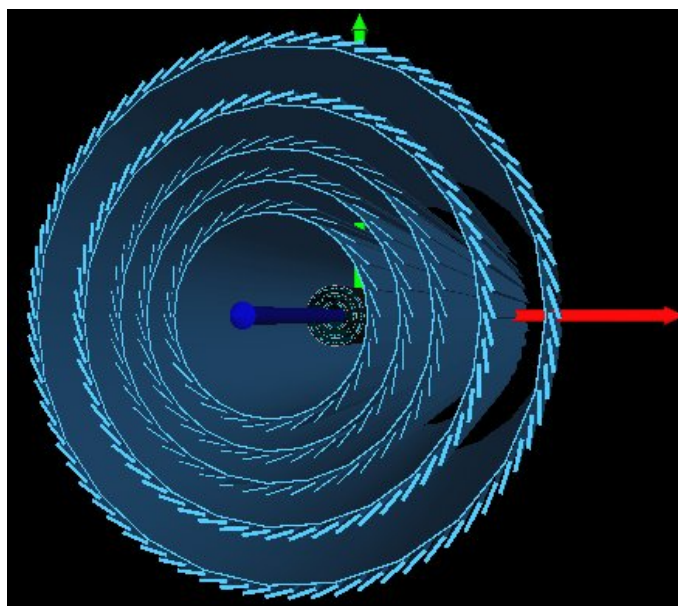


**Figure 2.9:** A 3D model of the upgraded SCT barrel [7].

Radius [mm]	380 / 501 / 622 / 743 / 1,000
Length [mm]	2355
Number of modules in $\phi$	28 / 36 / 44 / 52 / 72
Number of modules in $\eta$	96 (short strips) / 24 (long strips)
Gap between modules in $\eta$ [mm]	0.5
Modules in total	5,568

**Table 2.3:** Upgraded SCT barrel details.

## SCT Barrel Modules

A barrel module is composed of two sides glued on a base board, with shared read-out electronics. Each module side consists of 1280 silicon strips.

The pictures in figure 2.10 show the SCT module with the design that is currently being used in the ATLAS detector. The modules for the upgrade detector will in principle be similar, with some adjustments in the parameters. Figure 2.11 shows a sketch of a SCT module in the xy-plane. Table 2.4 contains details about the SCT module design.

To improve resolution in z-direction, it is considered to incline the strip directions by 40 mrad between the sides (stereo angle). However, the simulations for following studies have been performed with stereo angle turned off as it is obstructive in finding hit coincidences.

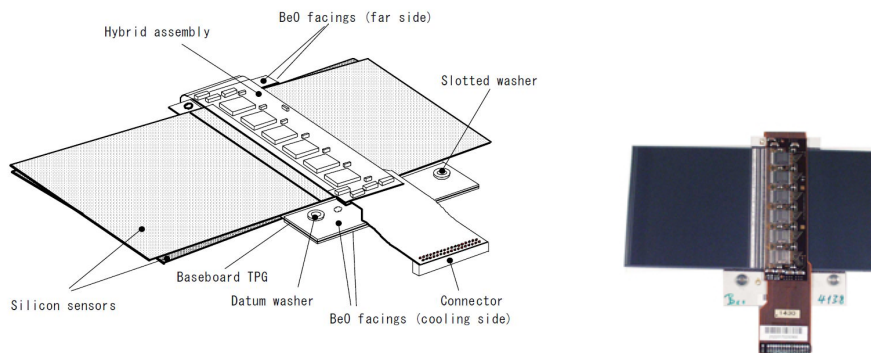


**Figure 2.10:** Figure and picture of the SCT module that is currently being used in the ATLAS detector (pre-upgrade) [3].

Width [mm]	100.0
Length [mm]	24.38 (short) / 97.54 (long)
Thickness [ $\mu\text{m}$ ]	320.0
Gap between sides [mm]	7.0
Strips per module side	1280
Tilt angle [degrees]	10

**Table 2.4:** Upgraded SCT module details.

## Silicon Strips

The SCT measures high resolution tracking information with the purpose of determining the particles bending radius in the magnetic field as well as to solve the

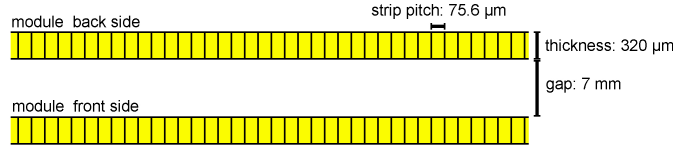


**Figure 2.11:** Sketch of a ATLAS-Upgrade SCT Module, in the xy-plane (not to scale).

combinatorial problem of track reconstruction. For momentum measurements, high precision perpendicular to the magnetic field (xy-plane) is required, while the resolution parallel to the magnetic field (z) is less significant.

The silicon strips of the SCT are designed accordingly: Very high granularity in the xy-plane but relatively long in z-direction, to avoid high costs and unnecessary amounts of read-out infrastructure. Shorter strips ( $\approx 2.5$  cm compared to  $\approx 10$  cm) will be used for the three innermost layers of the upgraded SCT, to countermeasure the increased detector occupancy. Table 2.5 shows geometrical details of the silicon strips.

Thickness [ $\mu\text{m}$ ]	320.0
Length [mm]	24.38 (short) / 97.54 (long)
Pitch [ $\mu\text{m}$ ]	75.6

**Table 2.5:** Upgraded SCT strip details.

## 2.5 Transverse Momentum Determination at Module Level

With increasing sensor occupancy, bandwidth limitations at the front end system become an important issue for the planned Level 1 Track-Trigger. This problem could be solved by filtering out hits originating from low- $p_t$  particles before track matching. For this thesis, the  $p_t$ -threshold for the hit selection is set to 10 GeV/c.

In addition, the preselection of data used for pattern matching is likely to cause a reduction of falsely matched tracks (fakes).

In the following section, two methods are introduced that can be utilized to discriminate hits originating from low and high- $p_t$  particles before read out at the frontend.

### Cluster Size

Depending on its transverse momentum, a particle might be sufficiently deflected by the magnetic field to hit two or more adjacent strips when crossing a module side. The cluster size is defined as the number of adjacent sensors that detected the particle (fig. 2.12).

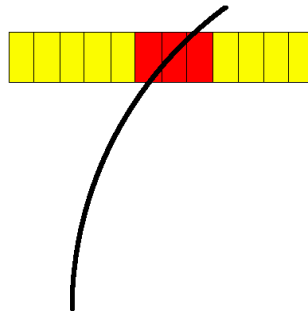


**Figure 2.12:** Cluster size method: a low momentum particle gets detected by 3 adjacent strips.

One can expect a hit with a high cluster size to be more likely originating from a particle with low  $p_t$ , which may be exploited for a preselection by rejecting hits above a certain cluster size threshold. In software, the cluster size is an information stored in the Raw Data Objects (RDO)<sup>3</sup>, i.e. a particle detected by three adjacent strips is still considered as only one hit by the detector output and stored as one entity.

---

<sup>3</sup>see appendix A.3 and section 3.1

## Double Layer Coincidence Offset

Due to the double layer structure of the SCT modules, a particle traversing one module will most likely get detected once on each side. Coincidences of two hits originating from the same particle can be built. Depending on the bending in the magnetic field, there will be an offset between the front and back side hit (fig. 2.13).

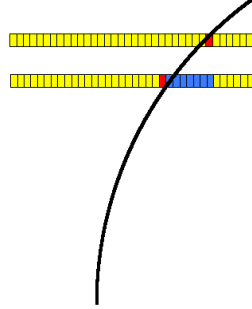


**Figure 2.13:** Offset method: due to bending in the magnetic field, the particle is detected with an offset of 7 (blue) between the hits on front and back side (red).

Similar to the cluster size, this hit offset can be put in correlation with the transverse momentum of the particle for a preliminary  $p_t$ -selection.

Because the travel distance of the particle in the magnetic field is roughly 20 times higher for the offset measurement (module side thickness compared to gap between sides), one can expect to get more distinct values in a larger range compared to the cluster size. The downside is that a correlation between two hits is needed, which is technically more demanding and might cause accidental coincidences at high detector occupancies.



## 3 Upgrade Detector Simulation

This section gives a short overview about the ATLAS simulation software as well as a presentation of the data sets used in the studies.

### 3.1 Detector Simulation Software

All data used in following studies have been generated using the ATLAS simulation software [8]. This software uses the GEANT4 [10] simulation toolkit and provides a detailed simulation of the ATLAS detector with variable detector geometries.

The simulation is divided into three steps [5]:

- event generation and immediate decays,
- simulation of interactions and detector response,
- digitization of the energy deposited in the sensitive regions of the detector.

The output data of the simulation can either be object based or identical to the output of the ATLAS DAQ. The latter allows both real data and simulation output to be run through the same trigger and reconstruction software.

For following studies, we use Raw Data Objects (RDO), a format used before event reconstruction has taken place. This corresponds to the data type that is used for triggering.

An issue for the studies with Raw Data Objects is that the simulation does not provide a link between truth information and the RDO data. As shown in the simulation flowchart (fig. 3.1), the truth information and the digitization are processed in different branches and only linked after event reconstruction. Therefore it is impossible to assign truth information of a particle to a single hit (i.e. RDO) caused by the particle. This makes it difficult to evaluate cut decisions when using events with more than one particle (secondary particles, pileup events).

### 3.2 Data Samples

The data samples utilized in our studies can be categorized in two sets serving different purposes: single particle events and minimum bias events.

In the following, all stated  $p_t$  values are transverse momentum at generation time of the particles.

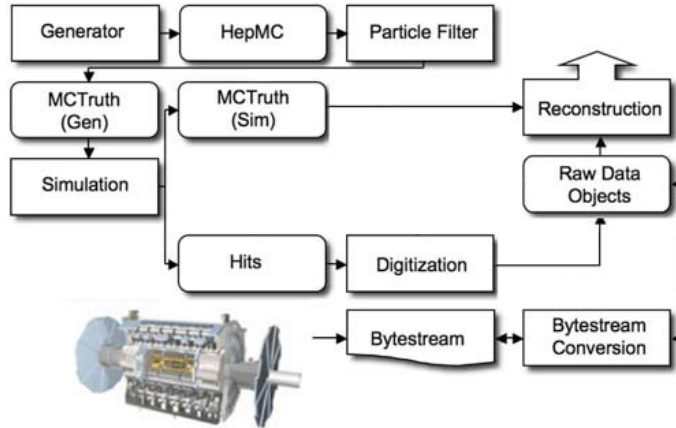


**Figure 3.1:** The flow of the ATLAS simulation software from event generation (top left) to reconstruction (top right). For our studies, the RDO format was used, which can also be converted from the detector output bytestream [5] (simplified).

### Single particle events

Single particle events are used for the analysis of cluster size and offset behaviour at defined transverse momentum values and hit positions. Because of their small interaction with matter, muons are best qualified for an unbiased understanding. Data sets with electrons and charged pions are used to study the consequences of energy loss, scattering and hadronic interactions.

Figure 3.2 shows the offset distribution measured from  $p_t = 1$  GeV/c hits at a 50 strips wide region of a module of the innermost strip layer, for different particles and detector configurations.

All of the shown distributions are for negatively charged particles. An energy loss in material and, through this, an increased deflection in the magnetic field is therefore expected to shift the offset, by definition towards positive values.

The first distribution shows offsets measurements for muons, with the pixel detector removed from the simulation. The distributions for muons *with* pixel detector and pions show a small shift of the average value to smaller offsets, the distribution for electrons however shows several outliers and a significant shift of the average.

As one would expect, muons and pions loose only little energy in interactions with the pixel detector material, while electrons, with inferior mass, are more susceptible.

The distributions of cluster sizes for different particles (fig. 3.3) provide qualitatively similar results, with electrons having a significantly higher average cluster size, and muons and pions showing a comparable behaviour.

Cluster size measurements with pre-upgrade SCT modules were performed in [12] and compared to simulation results (fig. 3.4). The results from measurement and simulation are consistent and match with the cluster size distribution of figure 3.3.

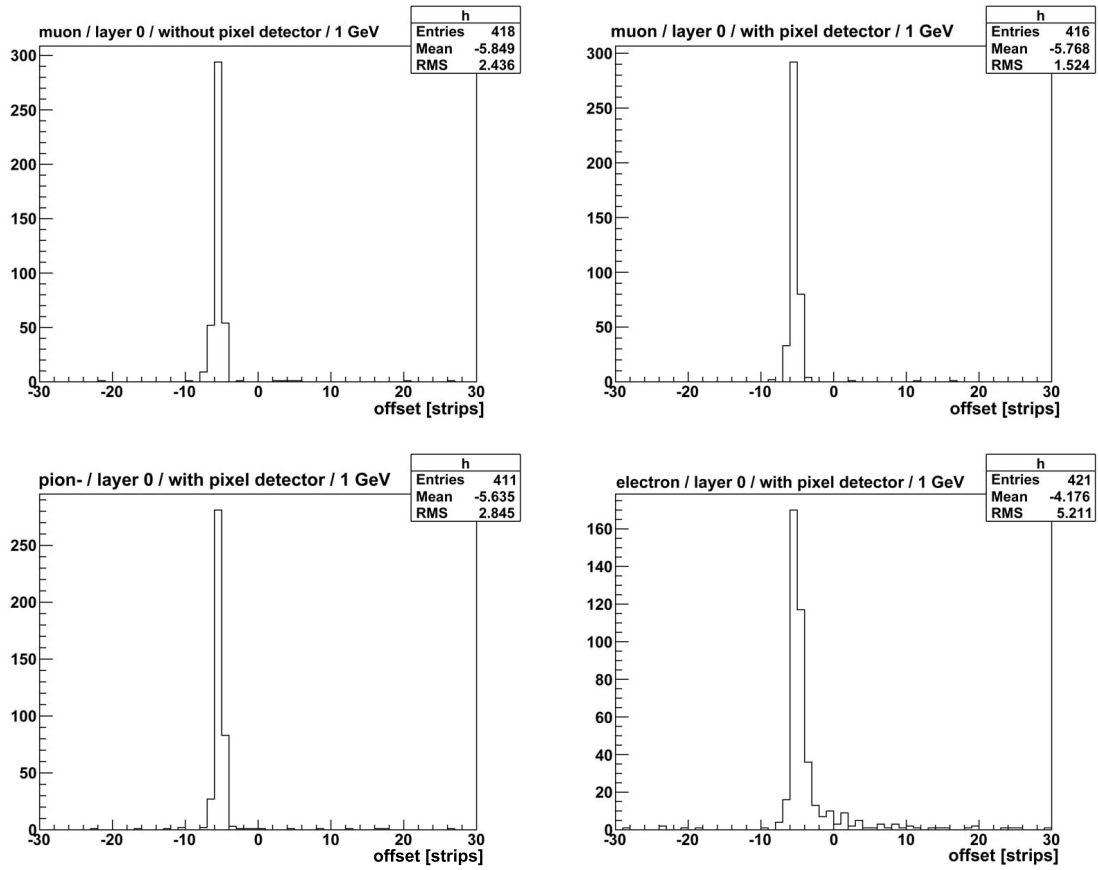


**Figure 3.2:** Offset distribution for different particles and detector configurations. Based on simulation data from hits in a 50 Strip wide region, at the center of a module of the innermost SCT layer.

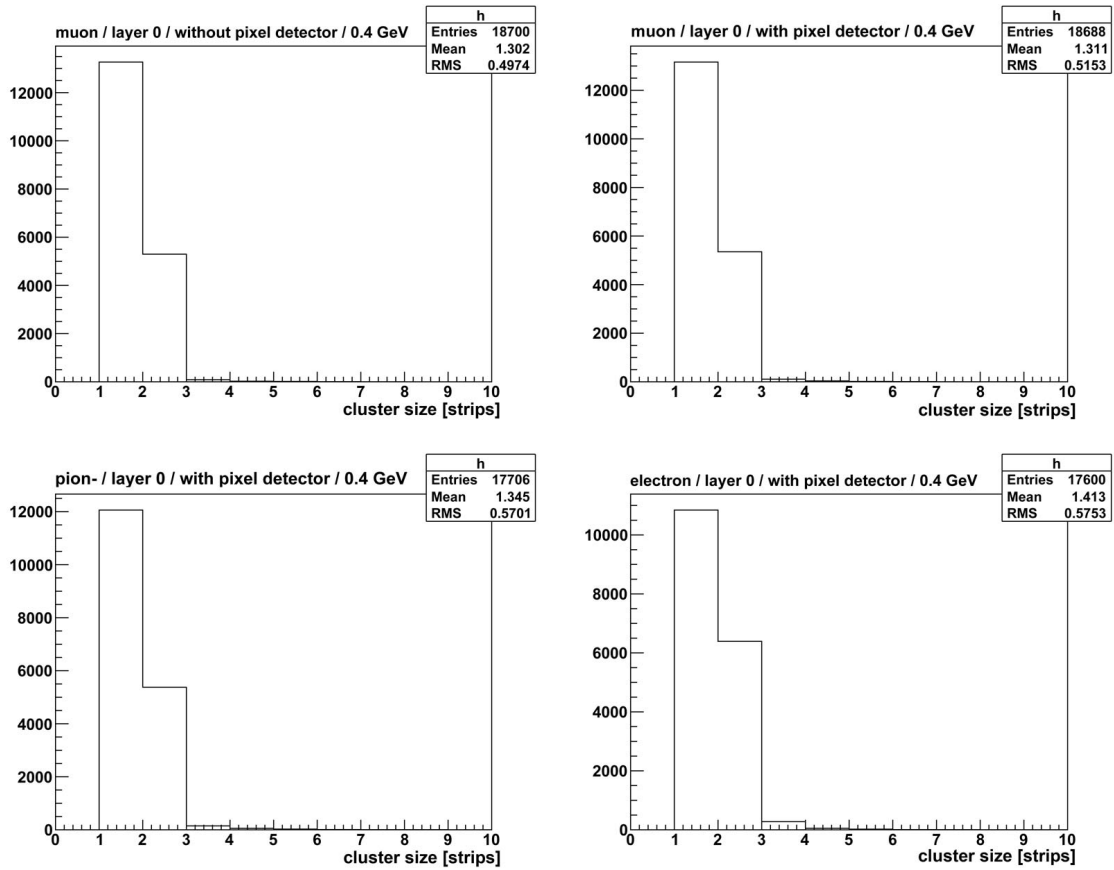


**Figure 3.3:** Cluster size distribution for different particles and detector configurations. Based on simulation data from hits on one module of the innermost SCT layer.

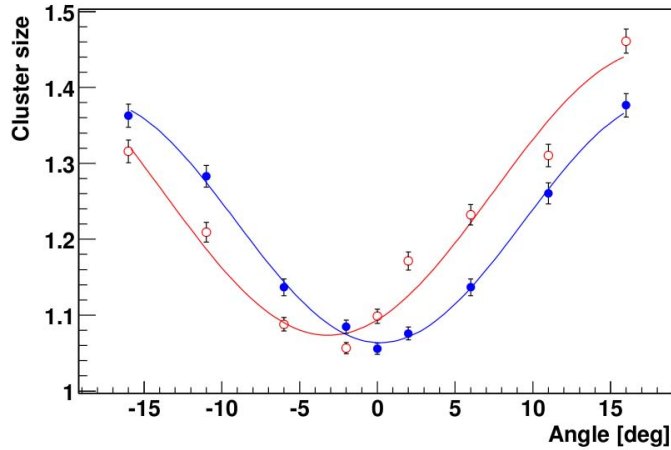


**Figure 3.4:** Cluster size versus angle of incidence, in a magnetic of  $B= 1.56$  T (open circles) and without magnetic field (full circles), measured with SCT barrel modules of the current ATLAS detector. Comparison with Geant4 and ATLAS SCT simulation (solid lines). The deflection of the particles in the magnetic field results in a shift of the measured cluster size [12].

### Minimum Bias Events

Minimum bias events provide a realistic particle composition and  $p_t$  distribution (fig. 3.5) and are used for data reduction estimations as well as other studies about the effects of pileup events.

The left plot of figure 3.6 shows the linear increase of the detector occupancy (average hits per module side) with increasing pileup. The single hit occupancy is smaller for outer layers, as the radial range of low  $p_t$  particles is limited by the bending in the magnetic field. It is higher for the two outermost layers however, as those are composed of long strips with a four times larger surface per module side.

The right plot shows the linear increase of the average amount of primary particles per event with increasing pileup.

### Number of Hits per Particle

Figure 3.7 shows the average amount of Raw Data Objects (i.e. hits), which muons, electrons and pions with a certain  $p_t$  cause in the SCT, as a function of transverse momentum. While this plot was calculated from single particle events, it also accounts for secondary particles generated in particle-matter interactions.

The overall behaviour for the three particle types is similar: for  $p_t < 400$  MeV/c particles curl in the magnetic field, resulting in a overproportional amount of hits, with a peak a  $\approx 250$  MeV. This peak is highest for muons, as they only slowly loose energy in detector material and therefore curl for a long time. Overall however, electrons cause most hits as they are more likely to emit bremsstrahlung.

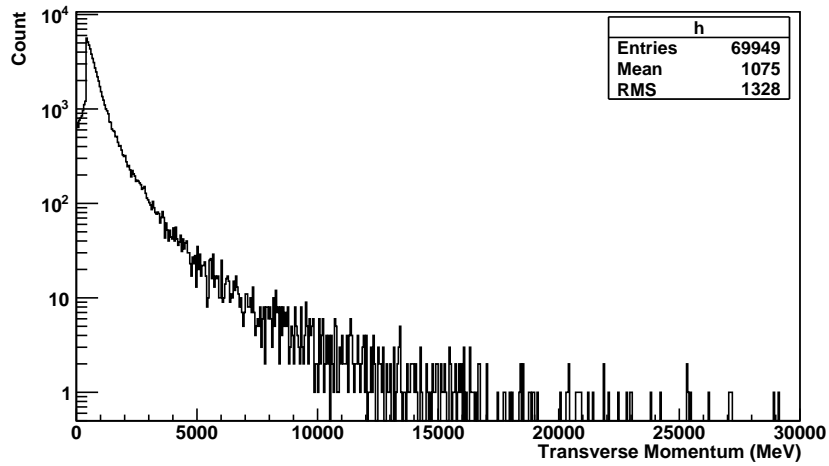


Figure 3.5: The  $p_t$ -distribution of a generated minimum bias data sample with 100 pileup events.

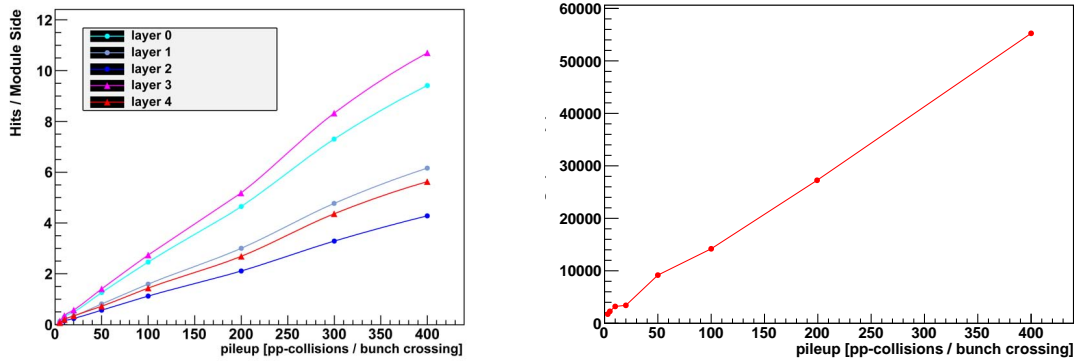
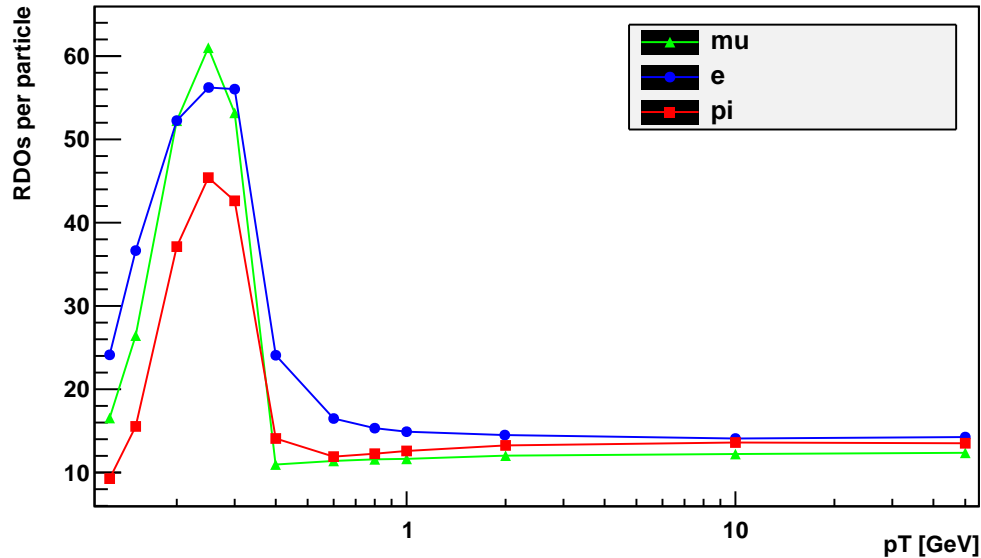


Figure 3.6: Average hits per module side versus pileup for the three short strip layers [circles] and the two long strip layers [triangles] of the SCT barrel (left). Average number of simulated particles per event versus pileup (right).

A particle with a high enough energy to leave the SCT detector without curling is detected at least 10 times, twice in each of the 5 double layers. The average is higher (muons: approximately 12 hits), which originates from secondary particles as well as from the module overlap (fig. 3.8).



**Figure 3.7:** Amount of Raw Data Objects a single muon, electron or pion produces in average in all 5 layers of the SCT barrel, for different transverse momentum.

### Secondary Particles

Secondary particles are generated in interactions of particles in detector material and have lower transverse momentum than the corresponding primary particle. Albeit being called single particle events, secondary particles are also generated in the simulation of this type of data, potentially influencing calculations based on measurement of cluster size and coincidence offset. Table 3.2 shows the occurrence of secondary particles in a simulated data sample with 20,000 muons and electrons at  $p_t = 50$  GeV/c.

Note that photons have no electric charge and are therefore not detected in the SCT detector.

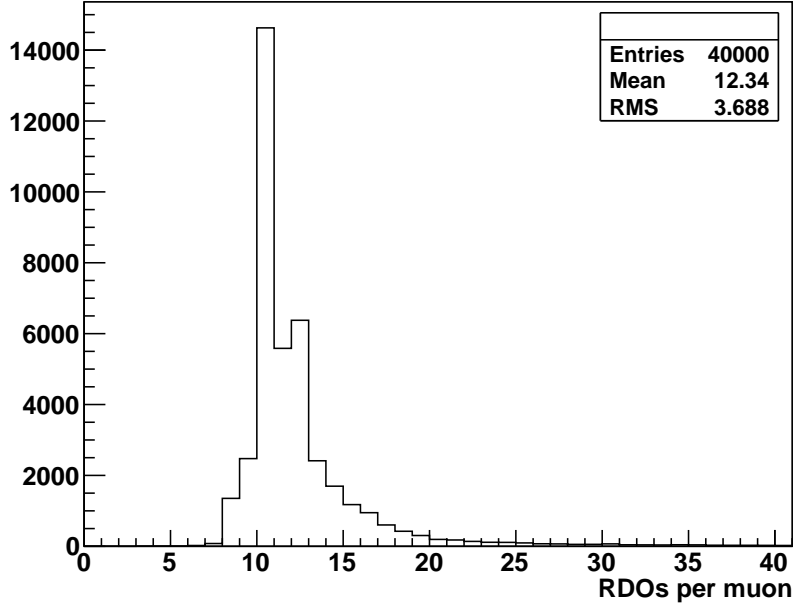


**Figure 3.8:** Distribution of the hits per muon with  $p_t = 10$  GeV/c. The second peak originates from the module overlap which causes two additional hits.

particle type	muons	electrons	pions
$e^-$	510	18,286	5,681
$e^+$	215	9,990	5,526
$\mu^-$	235	1	239
$\mu^+$	-	-	180
$\gamma$	75	30,093	28,038
$p^+$	-	171	9,713
$\pi^-$	-	-	471
total:	1035	58,541	49,954
percentage:	4.9%	74.5%	71.4%

**Table 3.1:** Number of secondary particles in a 50 GeV/c simulation data sample with 20,000 single  $\mu^-$ ,  $\pi^-$  and  $e^-$  events. Percentage of secondaries regarding the total amount of particles in the data sample. No restricted pseudorapidity range, as this makes a differentiation of primary and secondary particles impossible. The number of secondary particles with an  $\eta$  covered by the SCT barrel is significantly lower. Only photons with  $p_t > 1$  MeV/c are listed.

## 4 Offset and Cluster Size Dependences

In this chapter the different parameters influencing the cluster size and hit offset are described. The  $p_t$  ranges, in which these methods can be used for hit filtering are determined.

Single muon events are used, with the pixel detector removed from the simulation in order to prevent interferences, fake correlations and energy losses due to interaction with detector material.

Most of the plots in this section show measurements at the innermost detector layer. This layer can be considered as the most problematic one, because of its small detecting surface area and the proximity to the interaction point.

### 4.1 Transverse Momentum and Charge Dependence

Because the modules of the SCT are tilted by  $10^\circ$ , the bending direction and therefore charge sign causes particles to hit the module at different inclination angles, resulting in different measured cluster size (fig. 4.1) and hit offset.

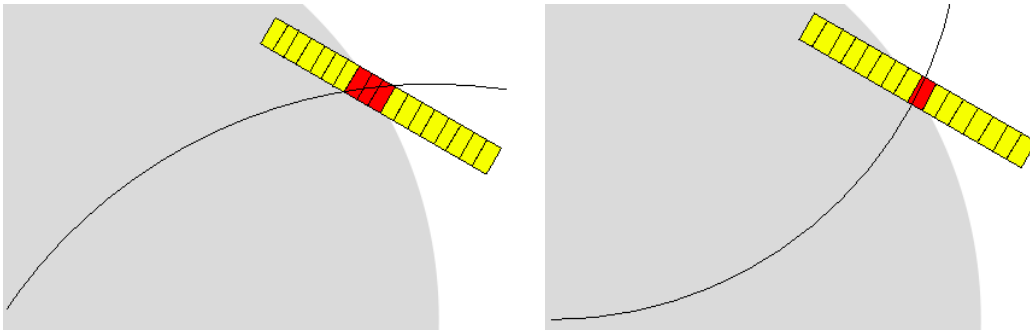


**Figure 4.1:** The measured cluster size (red) for two particles with same  $p_t$ , positively (left) and negatively (right) charged.

Muons and antimuons with a defined transverse momentum were shot uniformly distributed on a single module in the innermost layer of the SCT. The average resulting cluster size and hit offset for different  $p_t$  and both positive and negative charges are determined, based on the hits of 20.000 particles per parameter set. The error bars represent to the standard deviation of the measurement's distributions.

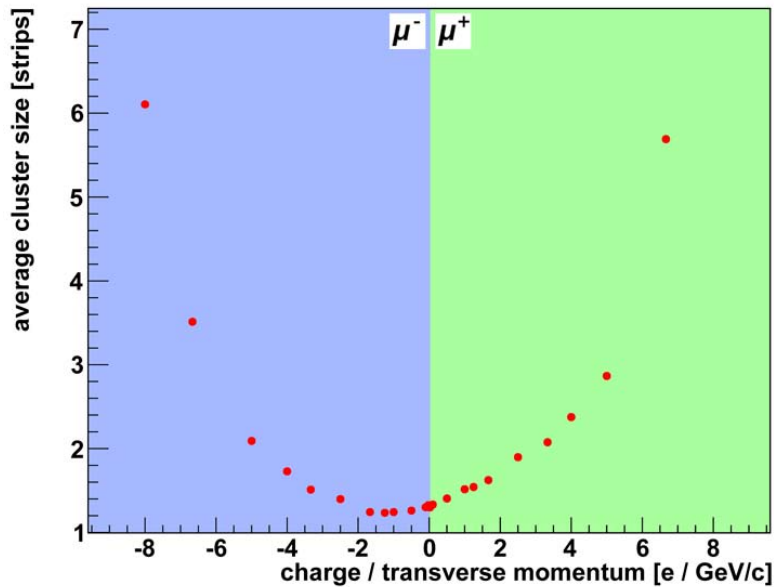


**Figure 4.2:** Cluster size versus charge sign over transverse momentum, measured at a module located in the first layer.

### Cluster Size versus Transverse Momentum

The dependence of the cluster size on the transverse momentum is shown in figure 4.2. As expected, the cluster size is large for small  $p_t$  values and vice-versa. Because of the tilt of the module, the parabola is tilted: positive charge causes higher cluster sizes for same  $p_t$  values. The minimal average cluster size is shifted to the left as muons with approximately 800 MeV/c ( $q/p_t \approx -1.25 \frac{e}{\text{GeV}/c}$ ) have a bending radius just right to hit the module perpendicularly, similar to the right picture of figure 4.1.

The plot gives a first idea about the  $p_t$ -range, where the cluster size method may be applicable for filtering out low momentum particles: because the cluster sizes of high  $p_t$  values all have an average very similar, between one and two, particles with  $p_t \gtrsim 250$  MeV/c can not be expected to be reliably distinguishable by this method.

## Offset versus Transverse Momentum

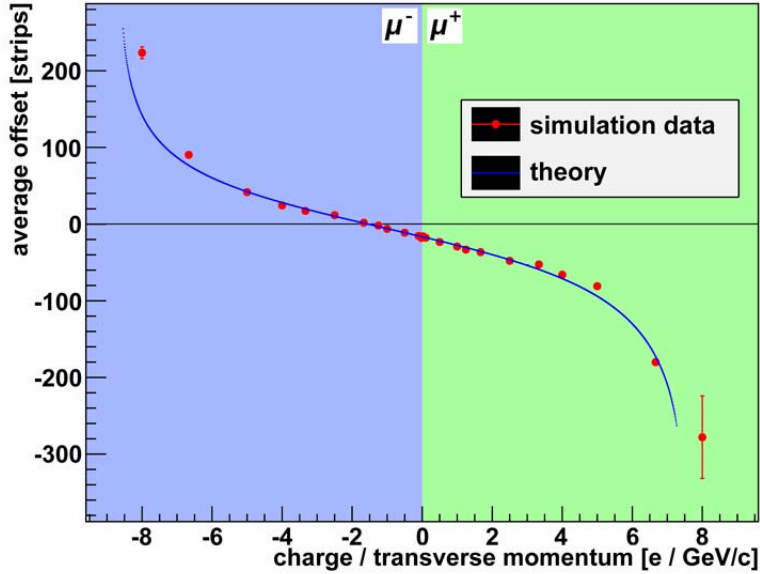


**Figure 4.3:** Double layer offset versus charge sign over transverse momentum, for the innermost layer. Comparison of simulation data (dots) and theory (solid lines).

The dependence of the double layer offset on the transverse momentum is shown in figure 4.3. The qualitative result is similar to the cluster size plot, with the difference, that negative offset values are possible. Still, as expected, the offset gets larger with smaller values of  $|p_t|$  and one can observe the same effects originating from the module tilt: positive charged particles result in higher offsets and the minimal absolute offset value is again located at approximately  $q/p_t \approx -1.25 \frac{e}{\text{GeV}/c}$ .

There is an important difference in the range of measured values however. Because of the distance between the two sides of the module (7 mm) being large compared to the thickness of one side of a module (285  $\mu\text{m}$ ), the deflection of the particle in the magnetic field is higher for the offset method, causing the measurement of more distinct values. Therefore, the offset method allows an overall better differentiation than the cluster size method, especially at high  $p_t$  values.

The plot in figure 4.3 also contains a curve showing theoretical offset values, calculated using geometrical considerations. These will be introduced in section 5.1. The results from the simulation match with the theory, except for the lowest  $p_t$  values. This deviation is caused by particles hitting the module front side but missing the back side because of their low energy and associated energy loss, resulting in low statistics. Particles hitting the module close to the edges are more likely to miss the back side. This results in fewer reconstructed offsets in these regions and therefore causing bias (see hit location dependence in next section).

## 4.2 Dependence on Module Impact Point

The distance from the origin of the particle to the hit, or in other words, the travel distance of the particle in the magnetic field, determines the angle at which a particle will hit a module. Therefore, particles with a certain  $p_t$  will have larger offsets and cluster sizes values with increasing radius of the detector layer.

Since the SCT modules are plane, not forming a perfectly barrel-shaped detector, as well as tilted, particles will traverse the modules at different angles, depending on the hit position in  $\phi$  direction (fig. 4.4). This results in a hit position dependence of the offset and cluster size, which has a non-linear component due to the varying travel distance in the magnetic field between primary vertex and front side and between front and back side. This non-linearity becomes relevant at small transverse momentum values.

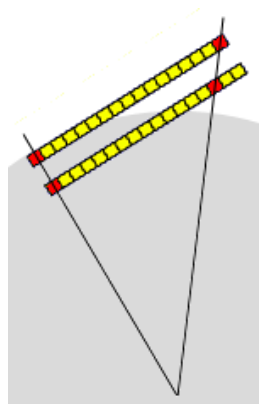


**Figure 4.4:** The measured offset depends from the location of the hit on the module.

For the next plots (fig. 4.5 and fig. 4.7), muons and antimuons with a defined transverse momentum were shot on a single module in the innermost layer of the SCT. The module was divided in 20 equally sized regions (64 strips per region, region width  $\approx 5$  mm, approximately 1,000 particles per region). For each region, the mean cluster size or offset was calculated separately. The error bars correspond to the standard deviation from the corresponding distributions. In order to check for consistency, the same was done with particles scattered over all modules in the first layer instead of only one module, with similar results.

### Cluster Size versus Hit Location

In Figure 4.5, one can recognize that the average cluster size is depending on the hit position on the module. However, this influence is rather small: the difference between hits on the far edges of the module is at most a half strip in average.

As a consequence of this dependence, we can expect a cluster size cut to affect varying  $p_t$ -ranges, depending on where the hit is located on the module. However, the influence is too small to set different cut thresholds for different regions.

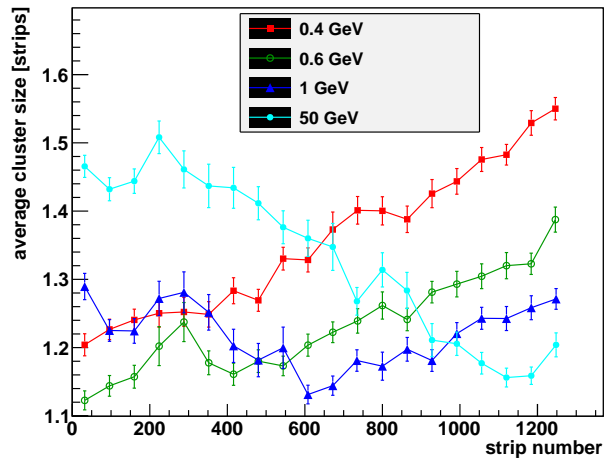
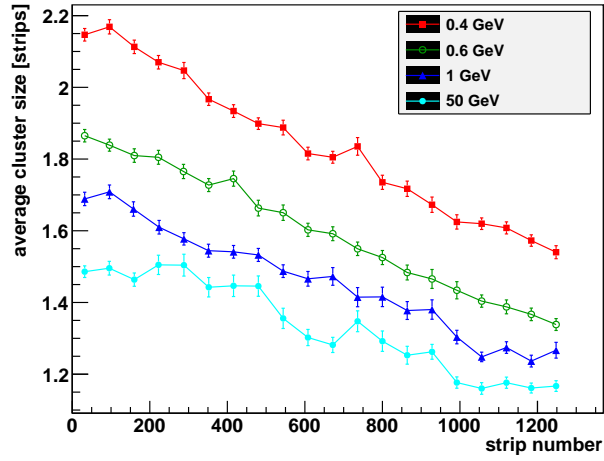


**Figure 4.5:** cluster size as a function of module hit position for  $\mu^+$  (top) and  $\mu^-$  (bottom), for the innermost layer.

The “turning point”, where track bending compensates for the tilt and the particle hits the module perpendicularly can also be observed in figure 4.5. For example, the slope of the 1 GeV/c graph for muons switches from negative to positive, resulting in a minimum at a hit position close to the module center. The slope of the graphs for low  $p_t$  muons is generally inversed (track bending overcompensating the tilt effect).

The amount of adjacent strips detecting a particle is not only dependent on the strip number but also on the location within the strip: depending on its charge sign, a particle penetrating a strip close to an edge will need more or less deflection to reach a neighbouring strip (fig. 4.6). As strips are the smallest detecting unit, this is an effect one cannot keep track on at measurement time. This is a statistical issue, which significantly influences the efficiency of a decision based on the cluster size. For the offset method, these fluctuations are less relevant because of the larger scope of measured values.

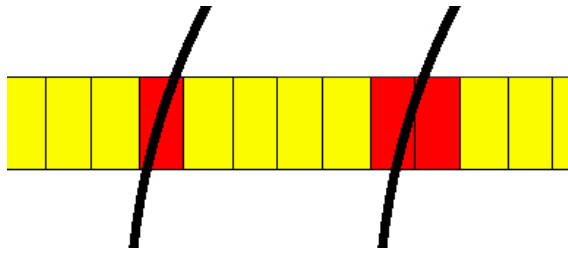


**Figure 4.6:** Two tracks with identical curvature radius and bending direction but different entering point result in a different cluster size.

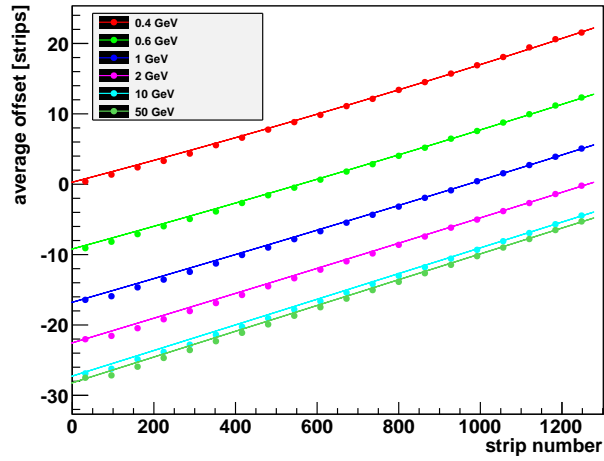
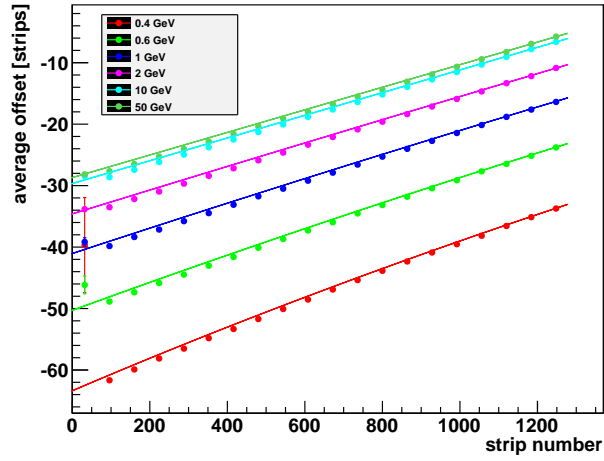
### Offset versus Hit Location

Figure 4.7 shows the hit position dependence of the offset. The overall characteristics of the offset behaviour are alike to the cluster size hit position dependency seen in figure 4.5: the absolute value of the offset gets smaller with increasing strip number, except for low  $p_t$  muons, which generate offsets  $\geq 0$  above a certain strip number by (over)compensating the base offset caused by the module tilt. The impact of the hit position dependency on the range of possible values is however much more important here, because of the larger scope of this measurement.

It becomes obvious that the discrimination of  $p_t$  by the offset is impossible without taking into account the hit location: there is a difference of 10 to 20 strips in average offset between the far ends of the module, while the average difference between the graphs for 1 and 50 GeV/c is of the same order.

Further to note, the 50 GeV/c curve is identical for muons and antimuons, just as expected because the tracks are effectively straight lines at such high  $p_t$  values.

The simulation results match satisfyingly with the theoretical calculations. There are some outliers for antimuons at low strip numbers, which is again caused by particles missing one module side.



**Figure 4.7:** Offset as a function of module hit position for  $\mu^+$  (top) and  $\mu^-$  (bottom), at first layer. Comparison of simulation data (dots) and theory (line).

### 4.3 Cluster Size Decomposition

After understanding which parameters influence the measurement results, the next step is to determine what information can be drawn from certain cluster size values in terms of the selection of high  $p_t$  hits.

In section 4.1, the influence of the transverse momentum on the *average* cluster size was shown. However, decision about single hits will not be based on averages. In order to make a conclusion from a certain cluster size value, one has to look into the decomposition of cluster sizes in dependency of transverse momentum.

The histograms in figure 4.8 show the occurrence of cluster sizes in percent, measured from muons and antimuons at a definite  $p_t$ . The data for each column is based on hits from 20,000 particles, evenly distributed on one specific module of the innermost layer.

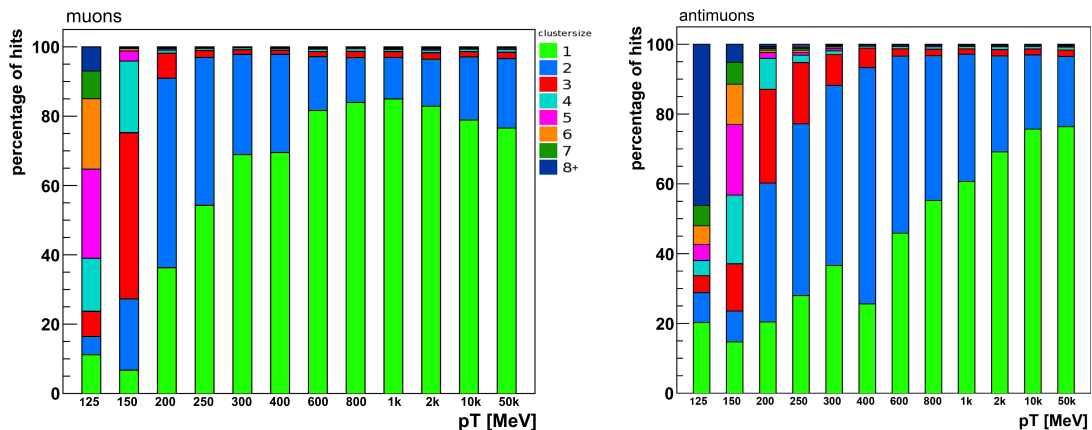


**Figure 4.8:** Histograms showing the decomposition of cluster size occurrences at different  $p_t$  values for the innermost layer.

No conclusion can be drawn from a measured cluster size of 1 and 2 as they significantly occur at all analysed  $p_t$  values. A cluster size above 2 is a strong indicator for a low momentum particle (muons:  $< 200$  MeV/c; antimuons:  $< 400$  MeV/c). Cluster sizes of three and more still occur at higher  $p_t$  at the scale of a few percent. The reason for this will be discussed in section 6.1.

Further, the histograms provide an overview of the data reduction rate that can be gained by applying cuts at specific cluster sizes. They also display the inefficiency of a cluster size cut: even at the lowest  $p_t$  values, cluster sizes of 1 and 2 occur at a non-negligible rate. This might be caused by detector inefficiencies.

A cut at cluster size  $\geq 3$  seems like the best compromise between data reduction rate and reliability; setting the threshold to  $\geq 4$  would roughly half the amount of wrong decisions, but at the same time lower the amount of rejected hits significantly by lowering the effective  $p_t$  threshold.

These histograms are in accordance with the previous plots, one can recognize

the already observed characteristics: the smallest cluster sizes are most likely to be found for negatively charged particles at  $p_t \approx 800$  MeV/c, and positively charged particles of the same  $p_t$  have larger cluster sizes.

Very large cluster sizes originate from particles that have a barely high enough transverse momentum to reach a specific layer. Ignoring the small influence of the module tilt, a particle requires  $p_t[\text{GeV}] \geq 0.3D[\text{m}]^1$  to reach a layer at the distance D from the vertex. Table 4.1 shows the minimum required  $p_t$  for the 5 layers of the SCT.

layer # (radius [mm])	required $p_t$ [MeV/c]
0 (380)	114
1 (501)	150
2 (622)	187
3 (743)	223
4 (1000)	300

**Table 4.1:** Minimal required transverse momentum required for a particle to reach a specific layer of the SCT.

The cluster size decomposition at outer layers looks likewise to figure 4.8, but for higher  $p_t$  values (fig. 4.9). Hence considerations about the cluster size threshold will lead to the same results. As a consequence, rejecting hits by cluster size affects different  $p_t$  ranges at different layers. As can be seen in figure 4.9, a cluster size cut threshold set to  $\geq 3$  rejects hits with up to 1 GeV/c.

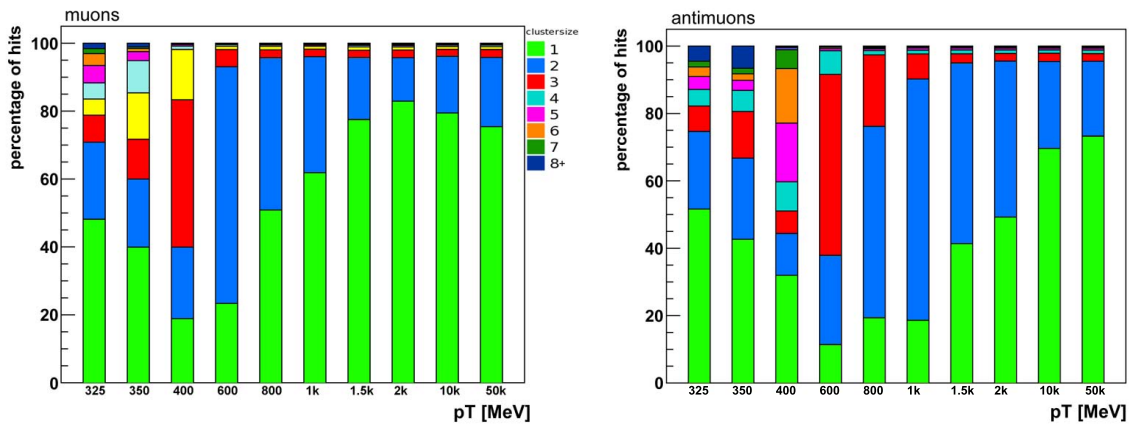


**Figure 4.9:** Cluster size decomposition for the outermost layer (1000 mm).

In summary, a cluster size cut has a varying and blurry range of effect. Particle in this range of effect however are produced in great numbers and curl inside the detector, causing an overproportionally high amount of unwanted hits (fig. 3.7).

<sup>1</sup>Derived from  $p_t[\text{GeV}] = 0.3BR[\text{m}]$ , with  $B = 2.0\text{T}$  and  $D = 2R$ .



# 5 Offset Cut Implementation

The offset is highly dependent on the hit position and requires a coincidence between two hits that needs to be reconstructed. Finding a corresponding hit is not necessarily unambiguous, especially with high detector occupancy. This chapter describes how a hit filtering, based on the coincidence offset could be implemented in the given environment. For such an implementation, a theoretical calculation of the offset that takes into account the hit position is required.

Measuring the cluster size and comparing it to a constant threshold is straightforward, in fact the cluster size is a value that is already read out in the SCT of the current ATLAS detector, being an information that is used for different purposes.

## 5.1 Theoretical Calculation of Coincidence Offsets

In chapter 4, it has been shown that, compared to the cluster size, the outcome of an offset measurement is influenced to a stronger degree by the hit position, due to geometrical reasons. We assumed that a selection based on offset needs to take into account where on the module the hit is located.

Therefore, in order to set an offset threshold for a  $p_t$  cut, a calculation of the offset in dependency of the expected hit location is required. This is also useful to verify results from simulation data, as it has already been done in previous plots (fig. 4.3, 4.7).

The calculation of the offset is a 2 dimensional problem, assuming the magnetic field is constant in z direction.

Assuming the front side hit coordinates as well as the transverse momentum and charge of the particle as given, the particle track can be parametrized as a circle. The cross section of the particle track and the module back side provides the coordinates for the back side hit. The offset is then calculated using the front and back side hit coordinates.

### Input Parameters

We assume the following parameters as given:

- transverse momentum  $p_t$ ,
- strip number [0-1279] of the frontside hit,
- particle charge sign,
- layer number [0-4],

along with geometrical constants: the module tilt angle  $\tau = 10^\circ$ , the gap  $g$  between the sides of the module, the strip pitch and the distance  $R$  from interaction point to the center of the module.

From above quantities we get the

- **track curvature radius**  $r_c = \frac{pt}{0.3B}$
- **distance from module center to hit**  $d = -(\text{strip number} - 640) \cdot \text{strip pitch}$
- **distance from vertex to module**  $R = 380, 501, 622, 743$  or  $1000$  mm

With those informations, we can calculate the coordinates of following points, with the origin of the coordinate system set to the vertex  $V$  (see fig. 5.1):

- **front side hit**  $H1 = (R + d \sin(\tau), d \cos(\tau))$
- **back side module center**  $M2 = (-g \sin(\tau), R + g \cos(\tau))$

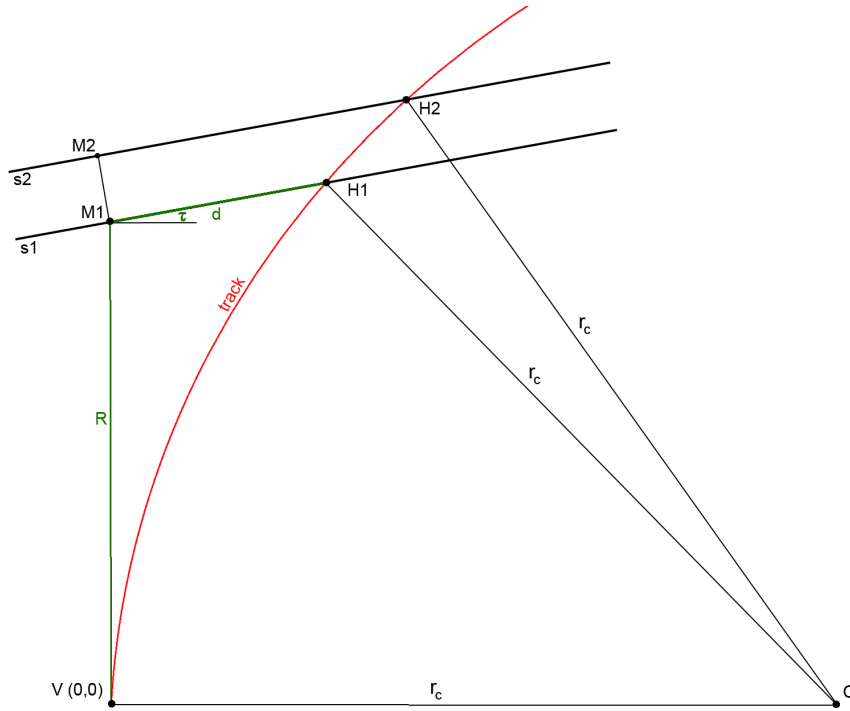


**Figure 5.1:** Calculation of the back side hit coordinates  $H2$ : the intersection point of the red circle (particle track) and the line  $s2$  (module back side).

## Track Parametrization

As a first step, we describe and parametrize the particle track as a circle and the module back side as a line, to calculate their intersections in order to get the back side hit coordinates.

The center point of the circle describing the track  $C = (x_0, y_0)$  can be calculated using the given curvature radius  $r_c$ :

$$(x - x_0)^2 + (y - y_0)^2 = r_c^2, \quad (5.1)$$

and two given points, the vertex  $V = (0,0)$ :

$$x_0^2 + y_0^2 = r_c^2 \quad \Rightarrow \quad y_0 = \pm \sqrt{r_c^2 - x_0^2}, \quad (5.2)$$

and the front side hit H1:

$$(x_{H1} - x_0)^2 + (y_{H1} - y_0)^2 = r_c^2 \quad (5.3)$$

$$\Rightarrow x_0 = \frac{\pm \sqrt{4r_c^2 y_{H1}^4 + 4r_c^2 x_{H1}^2 y_{H1}^2 - y_{H1}^6 - 2x_{H1}^2 y_{H1}^4 - x_{H1}^4 y_{H1}^2} + x_{H1} y_{H1}^2 + x_{H1}^3}{2(x_{H1}^2 + y_{H1}^2)}. \quad (5.4)$$

The solution of the quadratic equations can be obtained using the charge sign of the particle and geometrical considerations.

## Calculation of Back Side Hit Coordinates

The back side of the module is described as a line with a slope corresponding to the tilt angle  $\tau$ , running through the module center M2:

$$y = \tan(\tau)(x - x_{M2}) + y_{M2} \quad (5.5)$$

The particles hit position on the module back side H2 can be calculated as the intersection between circle (5.1) and line (5.5).

$$(x - x_0)^2 + (\tan(\tau)(x - x_{M2}) + y_{M2} - y_0)^2 = r_c^2 \quad (5.6)$$

$$\Rightarrow x_{H2} = -\frac{p}{2} \pm \sqrt{\frac{p^2}{2} - q}, \quad (5.7)$$

with

$$p = \frac{2(\tan(\tau)y_{M2} - \tan^2(\tau)x_{M2} - \tan(\tau)y_0 - x_0)}{1 + \tan^2(\tau)} \quad (5.8)$$

and

$$q = \frac{x_0^2 + y_0^2 + 2 \tan(\tau)x_{M2}(y_0 - y_{M2}) + \tan^2(\tau)x_{M2}^2 + y_{M2}^2 - 2y_0y_{M2} - r_c^2}{1 + \tan^2(\tau)}. \quad (5.9)$$

$$y_{H2} = \tan(\tau)(x_{H1} - x_{M2}) + y_{M2}. \quad (5.10)$$

Again, we need the particles charge sign to determine the correct solution.

### Offset Calculation

The offset can now be calculated from the x-coordinates of the front (H1) and back side hit (H2) (fig. 5.2):

$$o = \frac{x_{H2} - x_{H1}}{\cos(\tau)} \quad (5.11)$$

Finally, we get the offset in amount of strips  $o'$  with:

$$o' = \frac{o}{\text{strip pitch}}. \quad (5.12)$$

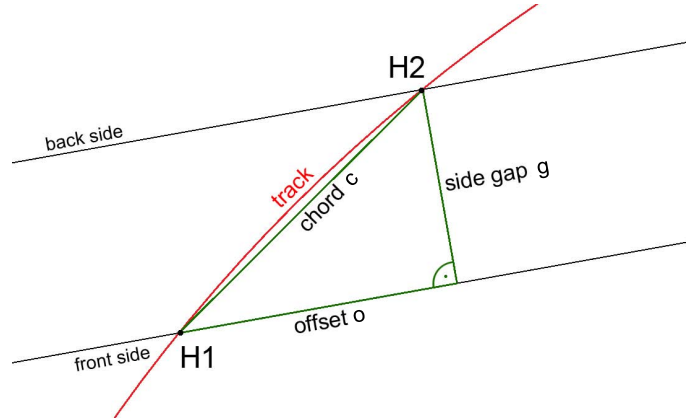


**Figure 5.2:** Calculation of the offset from the coordinates of the front and back side hits.

## Comparison of Theoretical Calculation and Data

Figure 4.3 and 4.7 show that the theoretical calculations satisfyingly describe the behaviour of the offset in dependency of the parameters. The scope of these plots however does not allow sufficient conclusions on the precision of the formula. The histograms in figure 5.3 show the distribution of the difference between theory and data results for muons with different charge,  $p_t$  and at different layers. The deviations are triangular distributed and are similar for all shown situations. For the majority of the data, the difference is between +1 and -1 strip, with only a few outliers.

As the difference is of at most one strip and the distribution is symmetrical around zero, the deviation between theory and data is of the same origin as for the cluster size distribution (see figure 3.6), the influence of the hit location within a single strip.

In figure 5.4, the distribution of deviations for pions and electrons is shown. For pions, the distribution is similar as for muons. For electrons, there are several outliers towards positive values aside the peak. The outliers for electrons mainly origin from bremsstrahlung. This can be concluded as they are all scattered on one side of the peak (radiative tail) as a consequence of increased deflection in the magnetic field. The behaviour of different particle types match with the observations made on the offset distributions, shown in the histograms in figure 2.3.

## 5.2 Validation Region

The readout electronics of the silicon strip detector do not provide the possibility for sophisticated processing. A relatively simple implementation of the offset cut is to validate hits by looking for hits in a certain region of the opposing side of the module (fig. 5.5). The limits of this region correspond to the two offset values (for positive and negative charge) of the  $p_t$ -threshold and can be calculated with the formula derived in the previous section. Due to the dependence of the offset on the impact point on the module, the validation region size is specific for every silicon strip. Because of the charge dependence of the offset as a result of the module tilt, the region is asymmetric around the position of a coincidence hit related to a straight track, as shown in figure 5.5. The distribution of the measured values in comparison with the theory (fig. 5.3) needs to be taken into account by broadening the region size by one strip in each direction. This is equivalent to lowering the  $p_t$ -threshold.

The hit validation method only requires compare logic and could be implemented using fast look-up tables containing precalculated region informations.

The simplicity of this hit selection makes it susceptible to wrong validations: a low- $p_t$  hit may falsely be validated by another random particle that incidentally hits the corresponding region. Therefore, one has to expect a small drop in the hit rejection rate at high detector occupancies and pile-up.

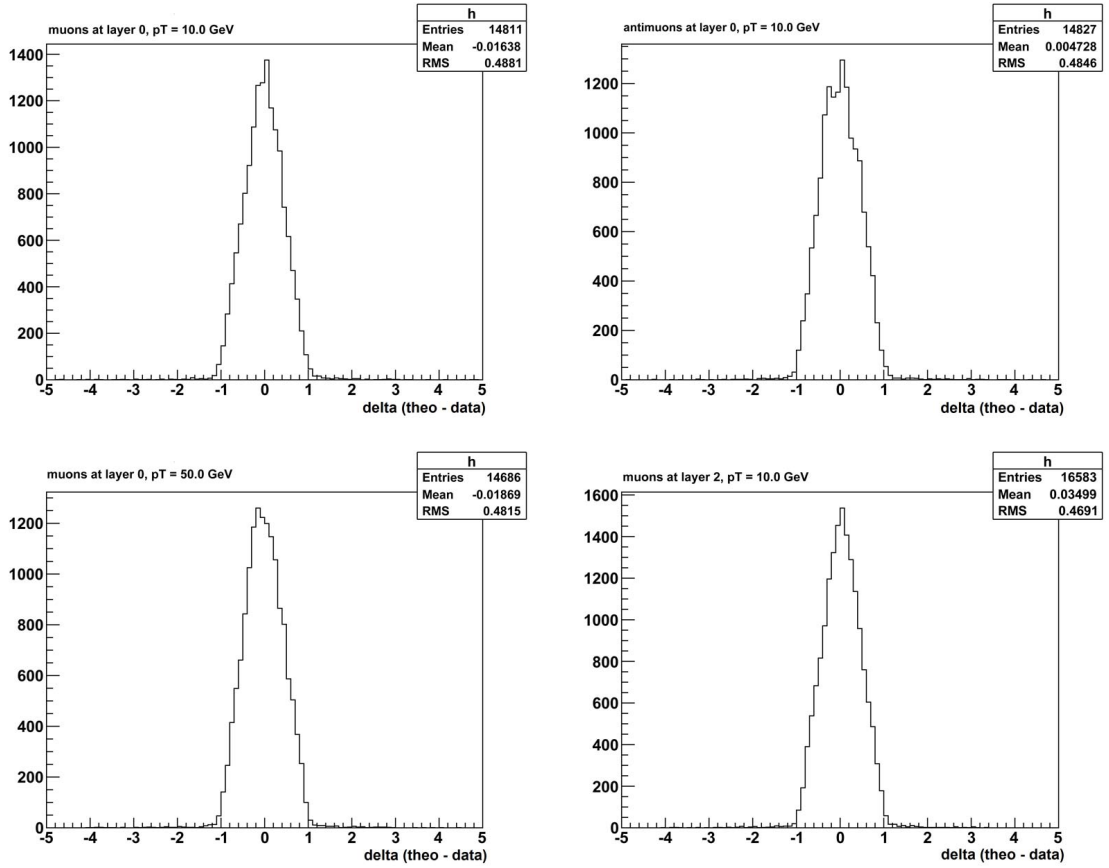


**Figure 5.3:** Distribution of the difference (in strip widths) between theoretical offset calculations and results from simulation data for muons with different charges,  $p_t$  and at different layers.

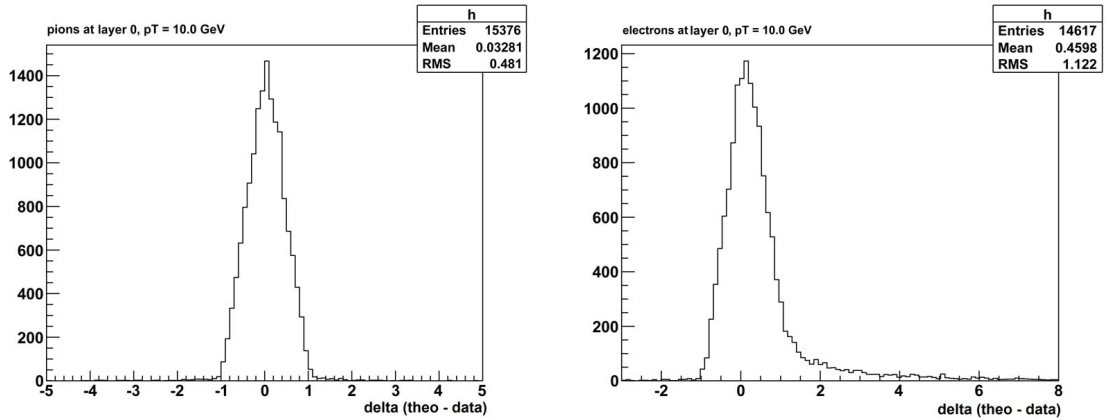


**Figure 5.4:** Distribution of the difference between theoretical offset calculations and results from simulation data for negatively charged pions (left) and electrons (right) with  $p_t = 10$  GeV/c, at the innermost layer.

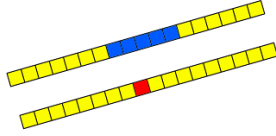


**Figure 5.5:** For every strip (red), a validation region (blue) on the opposed side is calculated. The validation region is asymmetric around the strip on the opposing side a straight track would hit, because the module tilt causes different offsets for positive and negative charge.

The validation region size is inversely proportional to the  $p_t$ -threshold (fig. 5.6), as we search for smaller offsets when looking for high- $p_t$  particles. Thus, a higher  $p_t$ -threshold makes wrong validations less likely and weakens the pile-up issue of the offset method.

A similar way to implement an offset cut by hit validation, as well as algorithms that use a combination of cluster size and offset cuts to reconstruct lost hits are studied in [14].

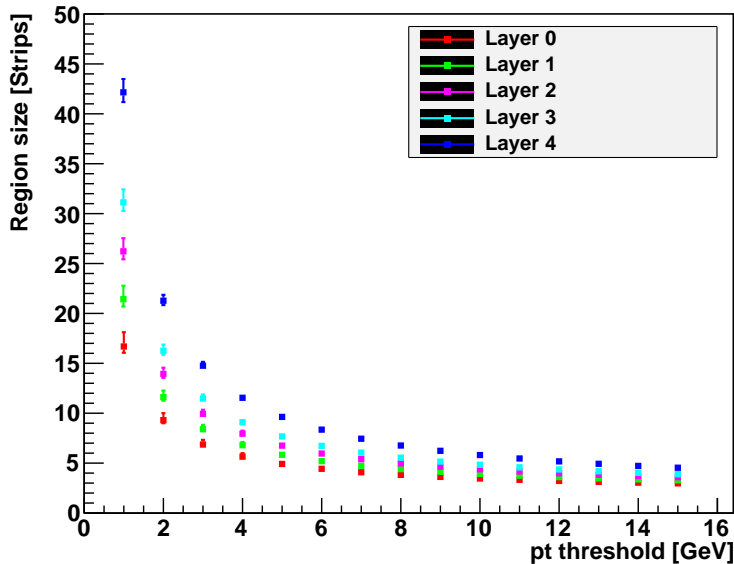


**Figure 5.6:** Validation region size versus  $p_t$ -threshold. The error bars display the varying size of the validation region (hit position dependency of the offset), the dots show the region size at the module center.

## Edge Recovery

Particles crossing a module close to one of its edges might cause that only one side is hit, with the corresponding validation region being (partially) off module. To resolve this, one can require the validation region to not surpass the module

borders before rejecting a hit. This edge recovery practically turns off the offset cut for strips close to the module edge, when no validating hit was found. By doing this, one trades missing validations with lowering the overall hit rejection rate for particles below the threshold. Missing the module back side after hitting the front side is more likely for particles with lower  $p_t$ . However the loss of a high  $p_t$  hit might have worse consequences for the track pattern matching than a slightly lower detector occupancy, therefore the special treatment of hits close to module edges seems reasonable and will be used in further studies. The effects of the edge recovery on the performance of the offset method is studied in section 6.1.

### Effect of Detector Inefficiency

Another cause for missing validations is detector inefficiency: a high- $p_t$  particle is detected at the front side, passes the validation region on the back side without being detected a second time, resulting in a misidentification. The SCT has a detecting efficiency of 99%.

An approach to reconstruct hits lost through detector inefficiency is discussed in [14]: The *combined algorithm* searches for the presence of a coincidence partner hit in a larger region (veto region), limited by the offsets of a particle that has a  $p_t$  just high enough to reach the corresponding layer (table 4.1). In case no coincidence partner is found, the hit rejection is vetoed and the hit is considered as an isolated high- $p_t$  hit. To avoid wrong coincidences caused by low  $p_t$ -particles as well as to reduce the size of the veto region, a cluster size cut is applied. However the cluster size turns out to be too unreliable for a reduction of the veto region size (fig. 4.8 and 4.9).

An issue with the *combined algorithm* is, that hits from low momentum particles curling in the magnetic field and only hitting one module side are more frequent than isolated hits due to detecting inefficiency. These hits look in principle like non-validated high- $p_t$  hits and would not be rejected anymore. Because of this, as well as inefficiencies at high amount of event pileup, the *combined algorithm* has not been implemented in further studies.

### Cross Module Communication

A particle with a sufficiently high pseudorapidity  $\eta$  may be displaced in z-direction to hit the front and back side of two different, adjacent modules (fig. 5.7). The likeliness for this linearly increases with increasing pseudorapidity and is lower for the two outermost layers, as they are composed of longer modules (10 cm instead of 2.5 cm). In the worst case (innermost layer, at the very far end of the barrel), more than 90% of the particles will hit the front and back side of two different modules (fig. 5.8). Therefore it is indispensable to check for validating hits not only at the current, but also at one additional adjacent module. The absence of such a cross-module communication would result in a large amount of missing validations, making the offset cut very unreliable in certain detector regions.

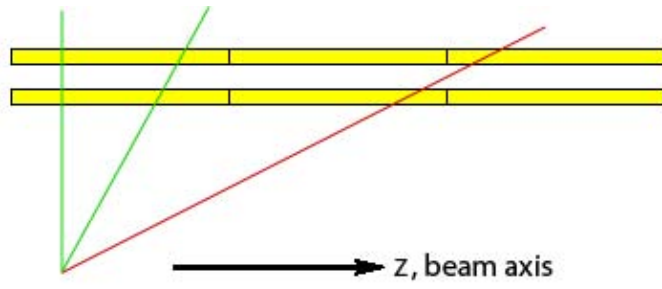


**Figure 5.7:** Depending on their pseudorapidity, particles are displaced by a certain distance in  $z$ -direction within the gap between the module sides. For high pseudorapidity, this may cause the front and back side hit to be on two different modules (red track).

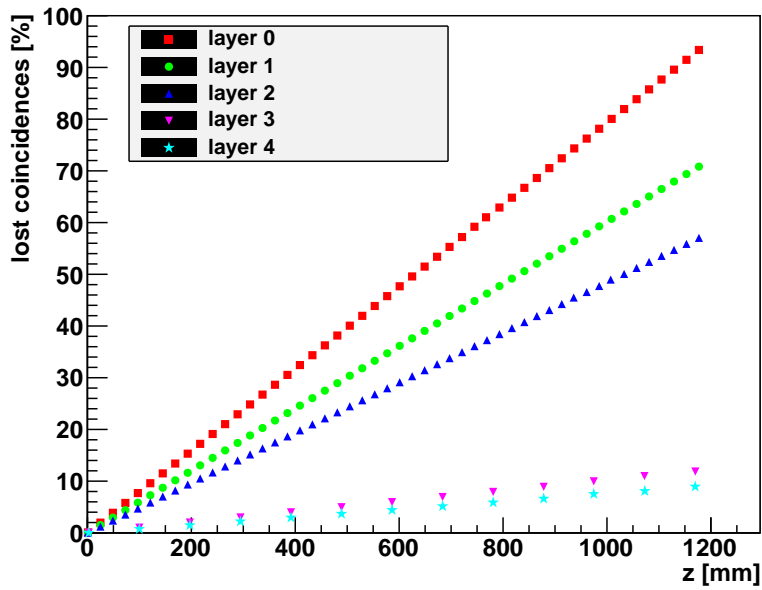


**Figure 5.8:** Percentage of lost coincidences without cross module communication versus module location in  $z$  (theoretical calculation).



## 6 Data Reduction Rates

In chapter 4 and 5, the options of setting thresholds for cluster size and offset based  $p_t$  cuts have been determined. This chapter contains studies about how precise these cuts operate and what threshold-specific data reduction rates can be achieved at certain particle  $p_t$ . The cuts are also applied on minimum bias events, to get an overall reduction rate estimation and in order to study the impact of pileup.

The reduction rate is defined as the percentage of Raw Data Objects (RDOs, the detector output corresponding to one hit) filtered out by the cuts.

Only the first three layers (short strips) are taken into account for the studies in this chapter.

### 6.1 Reduction Rate with Single Muon Events

The studies of the data reduction rate with single  $\mu^+ / \mu^-$  events with a fixed  $p_t$  allow a detailed insight into the behaviour and reliability of the cuts at specific thresholds.

In order to estimate the influence of secondary particle hits, two different sets of simulated data were used. The *full data* set contains hits from primary and secondary particles. As a distinction of hits from primary and secondary particle hits using Monte Carlo truth information is not possible (section 3.1), a selection of primary particle hits (referred as *only primary particles*) was done by requiring events to have a maximum of two hits per module (one hit per module side).

#### Performance of the Cuts at Different Thresholds

The graphs in figure 6.1 show the reduction rate of the offset cut with thresholds between 0.5 and 10 GeV/c and the cluster size cut with a threshold of 2 and 3, processed on single muon events with distinct  $p_t$  values. Only events without secondary particles were used.

For the offset graphs, the hit rejection rate starts at around 97% for low  $p_t$  and then drops to approximately 2% as soon as the specific threshold is surpassed. The wrong validations decrease slightly for increasing particle  $p_t$ . For the two highest thresholds, the hit rejection rate starts to drop at a  $p_t$  below the threshold.

Higher thresholds generally result in a higher hit rejection above the thresholds, because of the validation region size being smaller, which makes missing validations due to scattering more likely.

A small validation region size is also the cause for the hit rejection rate to drop below the nominal threshold: the extension of the validation region described in

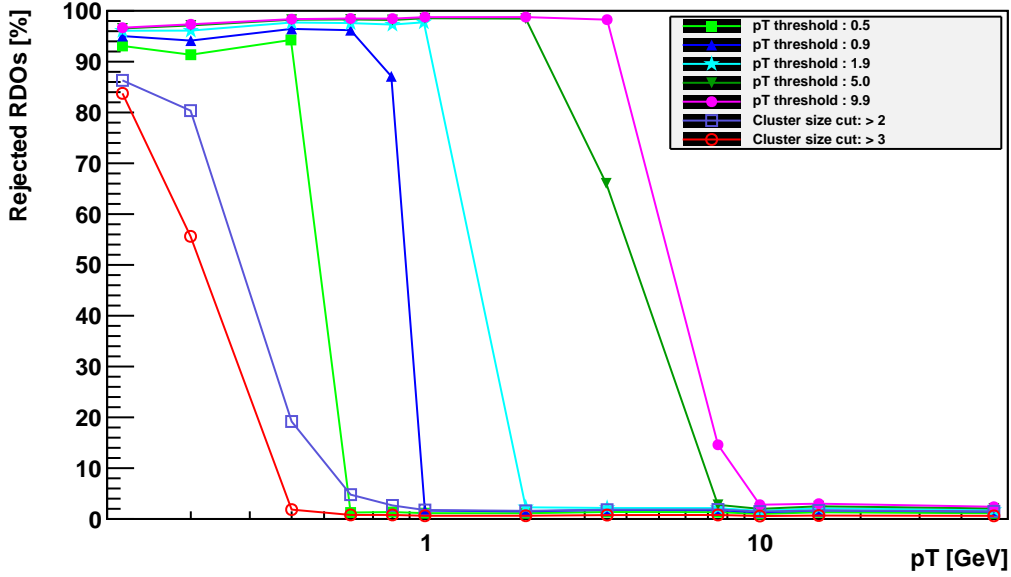


**Figure 6.1:** RDO reduction rate as a function of particle  $p_t$ , for offset and cluster size cuts at different thresholds, performed on single muon/antimuon events with an exclusion of secondary particles. Short strip layers only.

section 5.1, which is needed to take into account the deviation between theory and measurements, becomes important compared to the size of the validation region.

In the graphs for the cluster size cut  $> 2$  and  $3$ , the reduction rates start at  $\sim 90\%$  for  $125 \text{ MeV}/c$ , slowly dropping to approximately  $2\%$  and below  $1\%$  respectively at  $1 \text{ GeV}/c$ , further remaining at this rate for higher particle  $p_t$ . This behaviour matches well with the estimations drawn from the decomposition plots (fig. 4.8 and 4.9; note that the decomposition plots only show the cluster sizes for one layer.)

Table 6.1 contains hit rejection rates for cluster size and offset cuts with a threshold  $p_t < 10 \text{ GeV}/c$  for  $0.2 \text{ GeV}/c$  and  $50 \text{ GeV}/c$  (anti)muons. Particles with around  $0.2 \text{ GeV}/c$  cause most hits because of curling (fig. 3.7). For comparison, the table contains hit rejection rates of events with primary particles only, as well as for the full data set, showing the impact of secondary particles.

### Effect of the Edge Recovery

The edge recovery is supposed to prevent missing validations of particles hitting a module close to an edge, causing the validation region to be located (partially) off module. Table 6.1 shows a comparison of hit rejection rates with and without edge recovery.

For the hit rejection rate below the offset  $p_t$ -threshold, the edge recovery causes the amount of missing validations to drop. For  $50 \text{ GeV}/c$  muons, the hit rejection is relatively reduced by  $19\%$ , from  $2.4\%$  to  $1.9\%$ . Below the thresholds, the edge recov-

## Hit Rejection Rate

$p_t = 50 \text{ GeV}/c$ muons & antimuons	cluster size [%]	offset [%]
only primary particles	1.32	1.92
without edge recovery	1.32	2.38
full data	3.16	8.75
without edge recovery	3.16	10.30
<hr/>		
$p_t = 0.2 \text{ GeV}/c$ muons & antimuons	cluster size [%]	offset [%]
only primary particles	83.70	98.62
without edge recovery	83.70	100.00
full data	69.54	97.54
without edge recovery	69.54	99.85

**Table 6.1:** Comparison of the hit rejection rate of hits in percent for cluster size cuts ( $> 2$ ) and offset cuts (10 GeV/c) with or without edge recovery, applied to 50 GeV/c and 0.2 GeV/c muons. Two data sets were used: full data and a selection of events with only hits from primary particles. Short strip layers only.

ery causes the hit rejection rate to drop by 2%. This can however be compensated by applying an addition cluster size cut, as shown in section 6.3.

### Sources of Cut Inefficiencies.

Even at very high particle  $p_t$ , the hit rejection rate does not reach 0%. For the offset cut, this is to some part caused by the detector inefficiency of the order of below 1% per strip: particles pass the validation region but are not detected.

Scattering and energy loss in interactions with detector material can also cause particles to miss the validation region or to cause hits with a larger cluster size. The offset cut is more susceptible to such disturbances, especially at high  $p_t$ -thresholds with small validation regions. High- $p_t$  particles however are less susceptibility to deflections, therefore the hit rejection rate slowly drops for increasing particle  $p_t$  for both cut methods.

The hit rejection rates above threshold for the full data sample (i.e. with secondary particle hits) are significantly higher (table 6.1), reaching up to 10% for the offset method. For a large part, this can be ascribed to hits directly caused by secondary particles. These hits are very likely to be rejected by the cuts, due to their lower  $p_t$  and the differing travel direction. Beside that, secondary particles can also lead to increased cluster sizes for hits of the primary particle as well as wrong validations.

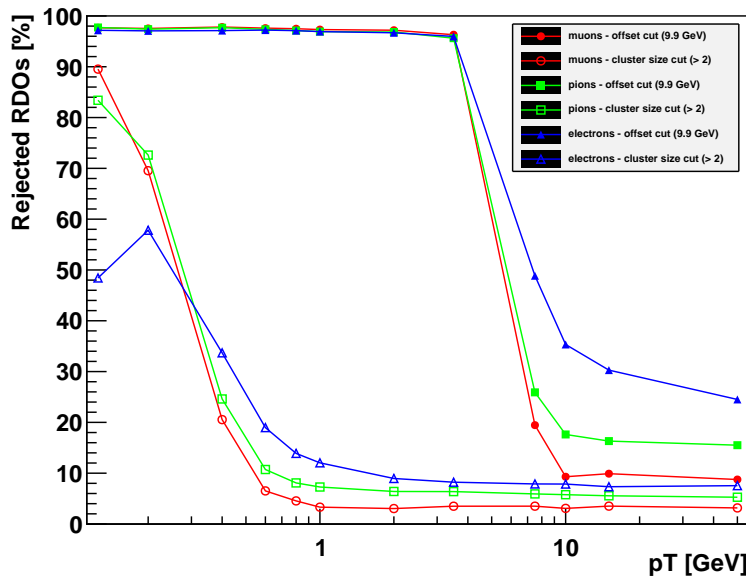
## 6.2 Hit Rejection Rate with Single Pion and Electron Events

Figure 6.2 shows the hit rejection rate of offset and cluster size cuts applied to single particle events with muons, pions and electrons. The plot also takes into account secondary particles, as limiting the data to events with only one hit per module side would reduce the amount data too much for pions and electrons. Table 6.2 shows hit rejection rates for the different particle types and different  $p_t$ .

For the offset method, the hit rejection rate below the threshold of 10 GeV/c is similar for all three particle types. The performance cluster size method however differs: while the hit rejection rate for pions is generally higher than for muons, it is lower for electrons with  $p_t < 200$  MeV/c. This might be caused by detector inefficiencies.

Above the threshold, the hit rejection rates for pions and electrons are significantly higher than for muons.

The overall higher hit rejection rate for electrons and pions is caused by the higher number of secondary particles (table 3.2) due to the stronger interaction of these particles with the detector material. With secondary particles, a high hit rejection above the threshold is not equatable with inefficiency, as the majority of the primary particle hits still pass the filter. For electrons, missing validations (fig. 3.2) and large cluster sizes (fig. 3.3) due to energy loss play an additional role.



**Figure 6.2:** RDO reduction rate as a function of particle  $p_t$ , for offset and cluster size cut performed on single particle events with muons, electrons and pions. This plot includes hits from secondary particles in contrary to the plot in figure 6.1. Short strip layers only.

### Hit Rejection Rate

$p_t = 50 \text{ GeV}/c$	cluster size [%]	offset [%]
$\mu^+/\mu^-$	3.16	8.75
$\pi^+/\pi^-$	5.27	15.51
$e^+/e^-$	7.55	24.51
$p_t = 0.2 \text{ GeV}/c$	cluster size [%]	offset [%]
$\mu^+/\mu^-$	69.54	97.54
$\pi^+/\pi^-$	72.61	97.68
$e^+/e^-$	57.82	97.06

**Table 6.2:** Comparison of the hit rejection rates of hits in percent for different particles. The cluster size cuts (cluster size  $> 2$ ) and offset cuts ( $p_t < 10 \text{ GeV}/c$ ) were applied to  $p_t = 50 \text{ GeV}/c$  and  $p_t = 0.2 \text{ GeV}/c$  single particle events. These values include hits from secondary particles. Short strip layers only.

## 6.3 Combined Application of Cluster Size and Offset Cut

### Hit Rejection Rate

$p_t = 50 \text{ GeV}/c$	os $\rightarrow$ cs [%]	cs $\rightarrow$ os [%]	cluster size [%]	offset [%]
only primary particles	2.84	3.85	1.32	1.92
full data	10.00	11.48	3.16	8.75
$p_t = 0.2 \text{ GeV}/c$	os $\rightarrow$ cs [%]	cs $\rightarrow$ os [%]	cluster size [%]	offset [%]
only primary particles	99.68	99.68	83.70	98.62
full data	99.10	99.09	69.54	97.54

**Table 6.3:** Hit rejection rates of hits in single muon events in percent, for different orders of application in a subsequent application of the cuts: offset cut applied before cluster size cut (os  $\rightarrow$  cs) or vice versa. Comparison of the combined application with individual application. Thresholds: cluster size  $> 2$ , offset:  $p_t > 10 \text{ GeV}/c$ . Short strip layers only.

Rejections of hits by Cluster size and offset are not necessarily correlated: for example, a back side hit from a particle might be located inside the validation region but, for some reason have a cluster size above the threshold. On the other hand, hits can get wrongly validated by a low- $p_t$  hit with a high cluster size. If one wants to filter hits with both the cluster size and the offset method, this leads to the question in what order the cuts should be applied.

Applying the cluster size cut first will reduce the risk of wrong validations at high detector occupancies but at the same time cause missing validations, leading to the loss of high- $p_t$  hits. By contrast, with the offset cut before the cluster size cut, the amount of wrong validations is expected to be higher, while the amount of missing validations is lower.

Figure 6.3 and table 6.1 show a comparison of the different orders of application in a subsequent application of cluster size and offset cuts (thresholds:  $cs > 2$ ,  $p_t < 10$  GeV/c) on single muon events with only primary particles. As there is no event pileup, only the benefits of an occupancy reduction by cluster size is not displayed and the initial application of the offset cut shows better results. Applying the cluster size cut first increases the hit rejection rate above the threshold twice as much relative to the individual offset cut application.

Below the threshold, the order of application has very little impact on the hit rejection rate. However one can expect the hit rejection rate to decrease slower at high pileup because of wrong validations, if the cluster size cut is applied first.

Figure 6.3 and table 6.1 also show a comparison of the performances of the subsequent applications with the performance of the individual application of cluster size and offset cuts. The graphs for the combined cuts only show slight improvements in contrast with the graph for exclusively offset cut. At very low  $p_t$ , the cluster size cut compensates for the previously described validation drop caused by the edge recovery, raising the hit rejection rate from 97% to more than 99%.

Comparing the subsequent plots with the offset-only plot, one might get the impression that the cluster size cut is redundant: the benefit for the hit rejection rate is small as both methods are based on the same principle, a hit rejected because of a high cluster size will also most likely have coincidence partner with a high offset. Additionally, the fake rate increases with a supplementary cluster size cut.

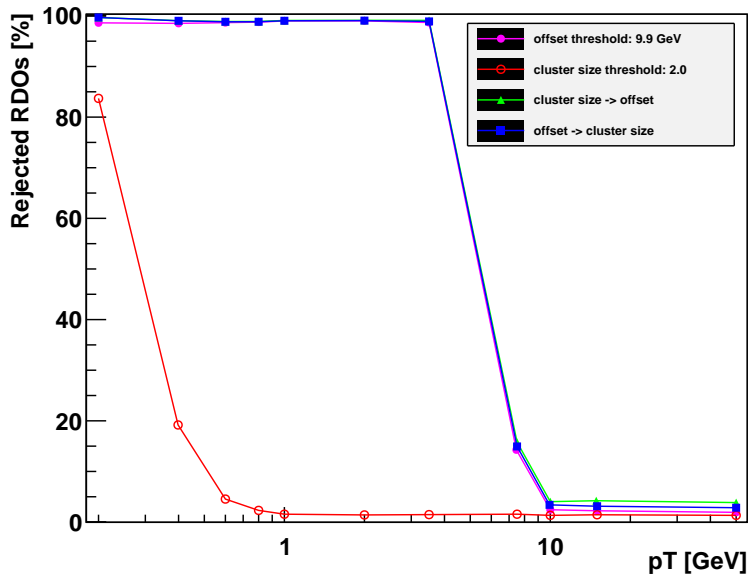
However, single muon events are an idealised environment. The major advantage of the cluster size cut, its reliability due to the lack of the need of a double layer coincidence will only show when applied on minimum bias data with event pileup.

## 6.4 Reduction Rate Estimation with Minimum Bias Events.

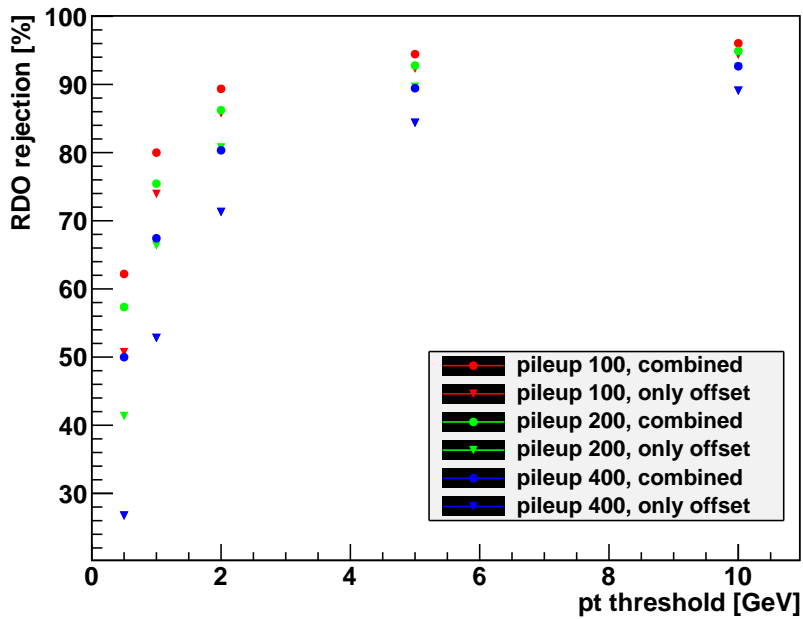
The previous section showed idealized reduction rates, based on selected single muon events with low matter interaction and no pileup, as well as a discrete  $p_t$  distribution. In order to estimate the overall achievable reduction rate, the cuts were applied on simulated minimum bias data, with the  $p_t$  distribution shown in figure 3.5.

Figure 6.4 shows the RDO rejection of the offset cut and of a subsequent application of the offset and cluster size cut versus the offset  $p_t$  threshold for different amounts of event pileup. The cluster size cut is set to reject hits with a cluster size above 2.

The hit rejection rate increases with increasing  $p_t$  threshold and drops with in-



**Figure 6.3:** Subsequent application of the cluster size and offset cut, in comparison with individual performance. Only hits from primary particles were considered for this plot. Short strip layers only.



**Figure 6.4:** Hit rejection rate versus offset threshold for different amounts of pileup, with and without cluster size cut (applied first). Short strip layers only.

creasing pileup. The difference between the hit rejection rates at different pileup declines with increasing offset threshold.

Pileup leads to higher detector occupancies (fig.3.6) and a low hit rejection rate due to the increased probability of wrong validations by other particles. A higher  $p_t$  threshold decreases the size of the validation region (fig. 5.6), which in turn lowers the probability of fake hit rejections.

A cluster size cut with threshold 2 by itself rejects approximately 36% of the RDOs (fig. 6.5). It is affected by pileup by a smaller degree, as the probability for two high transverse momentum particles hitting a sensor in such close proximity to form a single hit cluster remains small, even with a large amount of pileup events.

The benefit of a combination of the cuts is larger at lower  $p_t$  threshold because the disparity between the dependences on the amount of pileup increases with increasing validation region size.

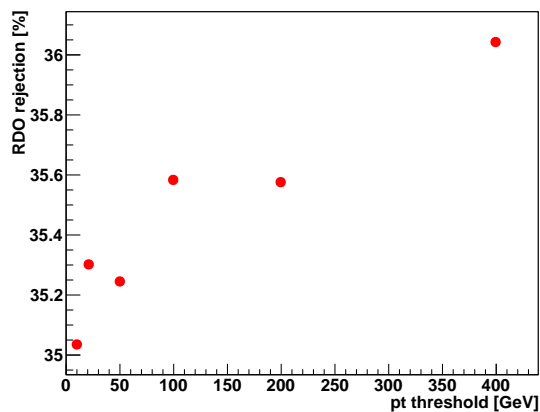


**Figure 6.5:** Hit rejection rate versus pileup in minimum bias events, for cluster size cut only. Short strip layers only.

## 6.5 Track Reconstruction

Beside lowering the bandwidth requirements for the track trigger, an important benefit of the hit filtering at module level is to decrease the fake rate of the pattern matching provoked by high occupancy. Because of the lack of a pattern matching simulation, the benefits from a cluster size and offset cut were estimated using a track fit. The employed track fitting algorithm is a non-iterative circle fit described in [15].

The cluster size cut and the offset cut are applied to simulated minimum bias data with different amounts of pileup. The high- $p_t$  coincidences found by the offset method are then used for track fitting with 6 hits (3 coincidences, one per layer). In case of an edge recovery, a 'coincidence' containing the same hit twice is used in order to have a full set of 6 hits.

The number of reconstructed tracks with a  $\chi^2$  below a certain threshold and a  $p_t$  above 10 GeV/c is compared with the number of corresponding particles in the Monte Carlo truth information.

Before applying the track fit to simulated minimum bias data, the track fit was normalised using single muon events.

### Track Fit Normalisation

The measurement error for the hits is set to  $\sigma_t = \text{strip pitch}$  (75.6  $\mu\text{m}$ ) in transverse direction, and to  $\sigma_l = \text{strip length}$  (24.38 mm) in longitudinal direction. A  $\chi^2$  threshold is then determined using 'ideal' 50 GeV/c single muon events with exactly 6 hits (two per layer).

Without hit filtering, 93.2% of the tracks are reconstructed. This matches the expectations: with the requirement of a full set of 6 hits for track fitting and a detector efficiency of 99%,  $(0.99)^6 * 100 = 94\%$  of the tracks are reconstructed. Deflections cause approximately 1% of the tracks to surpass the  $\chi^2$  threshold.

Cluster size (threshold:  $> 2$ ) and offset cut (threshold: 10 GeV/c) applied to the same data set reject 2.77% of the hits. With the chosen  $\chi^2$  threshold, 90.3% of the tracks are reconstructed after hit filtering. This is above the expected ratio of reconstructed tracks of 84.5%<sup>1</sup>, assuming the rejection of hits being independently distributed in all events. However this assumption is wrong, as the scattering of particles causes correlated hit rejections. Therefore, one can expect the amount of reconstructed tracks to be higher.

### Track Fit with Pileup

Using the setup determined with single muon event data, the track fitting algorithm was applied to minimum bias events with different amount of pileup. Before track fitting, cluster size (cluster size  $> 2$ ) and offset cuts ( $p_t > 10$  GeV/c) are applied to the data, resulting in a reduction of considered hits according to figure 6.4.

For every event, the number of reconstructed tracks with  $p_t > 10$  GeV/c and  $|\eta| < 1.4$  ( $\eta$  coverage of the first three layers of the SCT barrel) is compared with the number of corresponding charged particles in the truth information

Note that the missing link between truth and hit information makes it impossible to unambiguously evaluate the validity of a track reconstruction. The reconstructed track count does therefore not allow reliable conclusions about fake reconstructions and missed reconstructions and should rather be seen as a display of orders of magnitude.

---

<sup>1</sup>expected remaining tracks with a full set of 6 hits, if 2.77% of all hits are lost:

$$\left(\frac{100\% - 2.77\%}{100}\right)^6 = 0.845$$

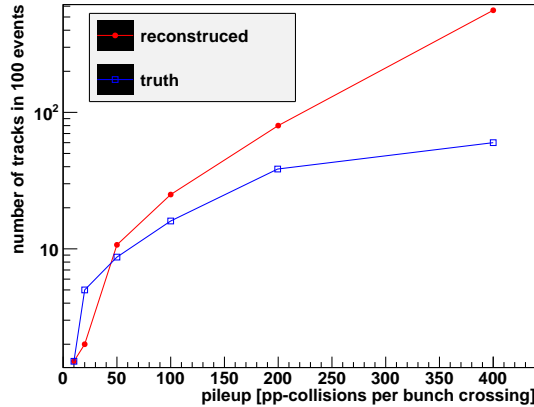


**Figure 6.6:** Number of tracks in 100 events with  $p_t > 10$  GeV/c and  $|\eta| < 1.4$  in the truth information of the simulation and from reconstruction via track fit, for different amounts of pileup.

A track fit with the full set of hits (without preselection) for comparison purposes could not be performed due to limited calculation capacity.

The number of reconstructed and expected tracks in 100 events is shown in figure 6.6, in dependence of amount of event pileup. At low pileup, the number of reconstructed high- $p_t$  tracks is smaller or equal to the tracks in the truth information. From pileup 50 on, the amount of reconstructed tracks starts to surpass the number of truth-tracks. At pileup 400, more than 550 high- $p_t$  tracks are found, a surplus of approximately 500.

Table 6.4 shows the percentage of events containing a reconstructed track with  $p_t > 10$  GeV/c.

The numbers at low pileup show, that a significant amount of the high- $p_t$  are not reconstructed, compared to the 90% reconstructed muons in single particle events. This is caused by the higher amount of wrong rejections at high pileup.

In some cases, single tracks are reconstructed multiple times by the fit algorithm. This happens for example because of the overlap of the module, causing two different coincidences in one layer to match. Multiple reconstructions can also be caused by fake matches at high detector occupancies. These multiple reconstructions lead to an accumulation of reconstructed tracks in single events containing a high- $p_t$  track and are not considered as one track in the counting.

Due to the uncertainties in these results, it is difficult to draw assumptions on the benefits of the hit reduction with the cluster size and offset method for pattern matching. Even with the discounting of multiple reconstructions, at 400 pileup events the amount of fake reconstructed tracks might be too high for triggering purposes with a threshold of 10 GeV/c. A further reduction of the detector occupancy might be required.

For a more reliable evaluation, a more detailed simulation of the pattern matching is required.

<b>pileup</b>	<b>events[%]</b>
10	1
20	1.5
50	5.3
100	10.0
200	35.0
400	95.0

**Table 6.4:** Percentage of the events containing at least one track with a reconstructed  $p_t > 10$  GeV/c.



## 7 Summary

With the planned luminosity upgrade of the LHC, the trigger system of the ATLAS detector will require improvements to furthermore ensure high performance. To achieve this, it is planned to introduce track reconstruction already at trigger level 1. The goal of a track trigger at level 1 is an early identification of high  $p_t$  tracks to identify e.g. leptons by using additional information from the calorimeter and muon trigger systems. This will allow to keep the trigger thresholds stable, while maintaining a reasonable trigger rate.

Due to bandwidth limitations, a preselection of high transverse momentum hits is required for the readout of data used for the track trigger. Two hit parameters from the silicon strip detector, the size of hit clusters and the transverse offset of double layer coincidences can be related with the transverse momentum of the particle. Based on these values, two methods referred as the *cluster size* and the *offset* method can be employed for a selection of high transverse momentum hits at front-end level. These methods have been analysed using a sophisticated detector simulation.

The influence of various parameters on the strip cluster size and the double layer offset have been studied: the transverse momentum and charge of the particle; the hit position on the module and the position within the detector.

The offset method is implemented using validation regions: a hit is considered as a valid, if a partner hit is found in a certain region on the opposing module side. Characteristics of this implementation are discussed.

It was found that the offset is more sensitive to parameter changes than the cluster size, due to geometrical reasons.

To test the performance at different  $p_t$ , cluster size and offset based cuts have been applied on single particle events. Below the  $p_t$  threshold, the offset cut rejects about 98% of the hits originating from the primary particles. Approximately 2.5% of the primary particle hits are rejected above the threshold, compared to 1.5% rejections of the cluster size cut. The cluster size cut rejects hits effectively up to 1 GeV/c. The performance of the combination of both methods was studied and different orders of subsequent application are compared.

The achievable hit rejection rate, as well as the influence of event pileup was determined using minimum bias events. The offset cut is more susceptible to pileup because of the increasing risk of wrong validations. The cluster size method is only slightly affected by pileup and can compensate some of the efficiency losses of the offset method at high pileup.

The number of reconstructed high- $p_t$  tracks after hit preselection has been estimated using a track fitting algorithm applied on minimum bias events with event

pileup.

The offset method has proven to be a capable way of selecting hits associated to high- $p_t$  tracks, while filtering out the majority of the unwanted hits. The cluster size method is less performant in terms of hit rejection rate, but is more reliable at high detector occupancies as it requires no hit coincidence. Both methods are combined and even in the most difficult scenario with 400 pileup events, a reduction of hits by 90% is achieved.

# A Appendix

## A.1 Luminosity

The Luminosity is an important value to describe the performance of a particle accelerator, allowing to calculate the expected event rate of a certain process with a given cross section  $\sigma$ :

$$\dot{N} = \sigma L \tag{A.1}$$

The luminosity has the unit  $\text{cm}^{-2}\text{s}^{-1}$ .

For a synchrotron like the LHC with identical beams in opposite direction, the Luminosity can be estimated by:

$$L = \frac{f_r \gamma N_b^2 n_b}{4\pi \epsilon_n \beta^*} F, \tag{A.2}$$

where

- $f_r$  is the revolution frequency
- $\gamma$  is the Lorentz factor  $\gamma = 1/\sqrt{1 - \beta^2}$
- $N_b$  is the number of protons per bunch
- $n_b$  is the number of bunches
- $\beta^*$  is the value of the betatron function at the interaction point
- $F$  is a factor describing the geometric loss due to bunches crossing each other at a certain angle ( $F < 1$ )
- $\epsilon_n$  is the normalized emittance, which is the volume the particle beam occupies in phase space. The normalized emittance is an invariant in Liouville's Theorem and thereby constrains the phase space evolution, i.e. the focusability of the beam.

The integrated luminosity

$$\mathcal{L} = \int L dt \tag{A.3}$$

is a value used to describe the amount of data that has (potentially) been taken by the detectors of an accelerator, usually given in  $\text{barn}^{-1}$ .

## A.2 The ATLAS Coordinate System

The coordinate system of ATLAS is right-handed, with the z-axis tangential to the LHC tunnel. The x-axis points to the center of the tunnel. The y-axis is slightly tilted ( $0.704^\circ$ ) with respect to vertical, because of a general tilt of the tunnel.

The pseudo-rapidity of particles originating from the vertex is defined as:

$$\eta = -\log \tan \theta, \tag{A.4}$$

with  $\theta$  being the polar angle of the particle direction.

The transverse momentum  $p_t$  is measured in the xy-plane, perpendicular to the beam (z-axis) and the magnetic field of the inner detector.

## A.3 The Detector Simulation Data Format

The detector simulation data output is stored in ROOT files. These files contain truth information about the simulated particles, as well as informations about single hits in the silicon strip detector, the Raw Data Objects (RDOs).

Following ROOT-branches were used in the studies for this thesis. Linking the information between the two categories (Truth and StripRDO, i.e. particle and hit) is not possible.

### Hit information:

- StripRDOStrip - the number of the silicon strip on the module [0-1279]
- StripRDOSide - the module side [0/1]
- StripRDOsize - size of the hit cluster
- StripRDOEtaModule - numbering of the module in  $\eta$  direction
- StripRDOPhiModule - numbering of the module in  $\phi$  direction
- StripRDOLayerDisk - layer [0-4]
- StripRDO\_x0 - Cartesian coordinates of the hit
- StripRDO\_y0
- StripRDO\_z0

### Truth information:

- TruthPx - component of the particles transverse momentum in x-direction
- TruthPy
- TruthPz
- TruthPdgId - particle type (monte carlo particle numbering scheme)
- TruthStatus - status of the particle

## A.4 Code Implementation of the Hit Validation

The python function emulating the hit filtering by double layer coincidence offset, used for the data reduction plots. The function gets information about a front side hit as input and searches for hits in the validation region of the module back side.

After a failed search for validating hits, the function checks if the validation region is (partially) off module and, if so, returns a single hit 'coincidence'.

The function `os_theo` calculates the offset for a given hit position, charge and transverse momentum with the formula derived in section 5.1.

```
def os_validation(layer, module, RDO, list_RDO, pt_threshold):

# input:
# - layer number
# - module id
# - RDO: index of the raw data object for the hit that is getting tested
# - transverse momentum threshold
# - list containing the RDOs from this event

# output:
# - a list of found coincidences

# split the module id
    phimod = int(module.split(':')[0]) # module phi number
    etamod = int(module.split(':')[1]) # module eta number

# set up a list containing the two adjacent modules that potentially contain validating hits

    if etamod <= 0:
        neighbourhood = [str(phimod) + ':' + str(etamod - 1), str(phimod) + ':' + str(etamod)]
    elif etamod > 0:
        neighbourhood = [str(phimod) + ':' + str(etamod), str(phimod) + ':' + str(etamod + 1)]

# calculate validation region

    Strip_0 = tree.StripRDOSTrip[RDO] # side 0 hit position
# largest strip number accepted (+ 0.5 for rounding, +1 for the theory-data deviation)
    max_strip = round(Strip_0 + offset(os_pt_cut, Strip_0, layer, charge = -1,
side_gap, strip_pitch, tilt_angle) + 0.5 + 1)
# lowest strip number accepted
    min_strip = round(Strip_0 + offset(os_pt_cut, Strip_0, layer, charge = +1,
side_gap, strip_pitch, tilt_angle) - 0.5 - 1)

    keepHit = False # reset flag
list_coincidences = [] # a list containing the RDO indices of found coincidences.

    for neighbour in neighbourhood: # loop over the modules that may contain a partner hit
        if neighbour in listRDO[layer]: # are there hits on these modules?
            if listRDO[layer][neighbour][1]: # if backside contains a hit
                for RDO_1 in listRDO[layer][neighbour][1]: # loop over back side RDO indices

                    Strip_1 = tree.StripRDOSTrip[RDO_1] # side 1 hit position

                    if Strip_1 > min_strip and Strip_1 < max_strip: # current hit is in the region?

                        validated = True
list_coincidences.append(RDO, RDO_1)
```

```

    if not validated:

# if the validation region is (partially) off module,
  don't make assumption and return a 1 hit coincidence

        if min_strip < 0 or max_strip > 1279:

# return a 'coincidence' tuple containing the front side RDO twice
list_coincidences.append(RDO, RDO)
        return list_coincidences

    return [] # the val region is on module, but contains no hits
else:
    return list_coincidences # hits have been found in the val region

```

## A.5 List of Figures

2.1	CERN - Overview of the CERN accelerator complex [9]. . . . .	11
2.2	The ATLAS experiment - cut-away view [6]. . . . .	14
2.3	The ATLAS Inner Detector - figure showing the three subdetectors [6].	15
2.4	The ATLAS calorimeter system - cut-away view [6]. . . . .	16
2.5	The ATLAS Trigger System - Overview [2]. . . . .	17
2.6	Two pictures of a simulation showing the tracks in the upgraded inner detector resulting from one bunch crossing, corresponding to a luminosity of $L = 0.2 * 10^{34} \text{cm}^{-2} \text{s}^{-1}$ (left, 5 collisions) and $L = 10.0 * 10^{34} \text{cm}^{-2} \text{s}^{-1}$ (right, 200 collisions) [1]. . . . .	19
2.7	Inner Detector of ATLAS Upgrade: 3D view (left) and figure of the xy-plane (right), showing the four pixel layers close to the beam lines and five SCT layers [7]. . . . .	20
2.8	Implementation of the hit pattern matching using a CAM for fast look-up [13] (simplified). . . . .	22
2.9	A 3D model of the upgraded SCT barrel [7]. . . . .	23
2.10	Figure and picture of the SCT module that is currently being used in the ATLAS detector (pre-upgrade) [3]. . . . .	24
2.11	Sketch of a ATLAS-Upgrade SCT Module, in the xy-plane (not to scale). . . . .	25
2.12	Cluster size method: a low momentum particle gets detected by 3 adjacent strips. . . . .	26
2.13	Offset method: due to bending in the magnetic field, the particle is detected with an offset of 7 (blue) between the hits on front and back side (red). . . . .	27
3.1	The flow of the ATLAS simulation software from event generation (top left) to reconstruction (top right). For our studies, the RDO format was used, which can also be converted from the detector output bytestream [5] (simplified). . . . .	30

3.2	Offset distribution for different particles and detector configurations. Based on simulation data from hits in a 50 Strip wide region, at the center of a module of the innermost SCT layer. . . . .	31
3.3	Cluster size distribution for different particles and detector configurations. Based on simulation data from hits on one module of the innermost SCT layer. . . . .	32
3.4	Cluster size versus angle of incidence, in a magnetic of B= 1.56 T (open circles) and without magnetic field (full circles), measured with SCT barrel modules of the current ATLAS detector. Comparison with Geant4 and ATLAS SCT simulation (solid lines). The deflection of the particles in the magnetic field results in a shift of the measured cluster size [12]. . . . .	33
3.5	The $p_t$ -distribution of a generated minimum bias data sample with 100 pileup events. . . . .	34
3.6	Average hits per module side versus pileup for the three short strip layers [circles] and the two long strip layers [triangles] of the SCT barrel (left). Average number of simulated particles per event versus pileup (right). . . . .	34
3.7	Amount of Raw Data Objects a single muon, electron or pion produces in average in all 5 layers of the SCT barrel, for different transverse momentum. . . . .	35
3.8	Distribution of the hits per muon with $p_t = 10$ GeV/c. The second peak originates from the module overlap which causes two additional hits. . . . .	36
4.1	The measured cluster size (red) for two particles with same $p_t$ , positively (left) and negatively (right) charged. . . . .	37
4.2	Cluster size versus charge sign over transverse momentum, measured at a module located in the first layer. . . . .	38
4.3	Double layer offset versus charge sign over transverse momentum, for the innermost layer. Comparison of simulation data (dots) and theory (solid lines). . . . .	39
4.4	The measured offset depends from the location of the hit on the module.	40
4.5	cluster size as a function of module hit position for $\mu^+$ (top) and $\mu^-$ (bottom), for the innermost layer. . . . .	41
4.6	Two tracks with identical curvature radius and bending direction but different entering point result in a different cluster size. . . . .	42
4.7	Offset as a function of module hit position for $\mu^+$ (top) and $\mu^-$ (bottom), at first layer. Comparison of simulation data (dots) and theory (line). . . . .	43
4.8	Histograms showing the decomposition of cluster size occurrences at different $p_t$ values for the innermost layer. . . . .	44
4.9	Cluster size decomposition for the outermost layer (1000 mm). . . . .	45

5.1	Calculation of the back side hit coordinates H2: the intersection point of the red circle (particle track) and the line s2 (module back side).	48
5.2	Calculation of the offset from the coordinates of the front and back side hits.	50
5.3	Distribution of the difference (in strip widths) between theoretical offset calculations and results from simulation data for muons with different charges, $p_t$ and at different layers.	52
5.4	Distribution of the difference between theoretical offset calculations and results from simulation data for negatively charged pions (left) and electrons (right) with $p_t = 10$ GeV/c, at the innermost layer.	52
5.5	For every strip (red), a validation region (blue) on the opposed side is calculated. The validation region is asymmetric around the strip on the opposing side a straight track would hit, because the module tilt causes different offsets for positive and negative charge.	53
5.6	Validation region size versus $p_t$ -threshold. The error bars display the varying size of the validation region (hit position dependency of the offset), the dots show the region size at the module center.	53
5.7	Depending on their pseudorapidity, particles are displaced by a certain distance in z-direction within the gap between the module sides. For high pseudorapidities, this may cause the front and back side hit to be on two different modules (red track).	55
5.8	Percentage of lost coincidences without cross module communication versus module location in z (theoretical calculation).	55
6.1	RDO reduction rate as a function of particle $p_t$ , for offset and cluster size cuts at different thresholds, performed on single muon/antimuon events with an exclusion of secondary particles. Short strip layers only.	58
6.2	RDO reduction rate as a function of particle $p_t$ , for offset and cluster size cut performed on single particle events with muons, electrons and pions. This plot includes hits from secondary particles in contrary to the plot in figure 6.1. Short strip layers only.	60
6.3	Subsequent application of the cluster size and offset cut, in comparison with individual performance. Only hits from primary particles were considered for this plot. Short strip layers only.	63
6.4	Hit rejection rate versus offset threshold for different amounts of pileup, with and without cluster size cut (applied first). Short strip layers only.	63
6.5	Hit rejection rate versus pileup in minimum bias events, for cluster size cut only. Short strip layers only.	64
6.6	Number of tracks in 100 events with $p_t > 10$ GeV/c and $ \eta  < 1.4$ in the truth information of the simulation and from reconstruction via track fit, for different amounts of pileup.	66

## A.6 List of Tables

2.1	Comparison of inner detector layouts. . . . .	21
2.2	Number of channels in the inner detector, before and after upgrade. . .	21
2.3	Upgraded SCT barrel details. . . . .	23
2.4	Upgraded SCT module details. . . . .	24
2.5	Upgraded SCT strip details. . . . .	25
3.1	Number of secondary particles in a 50 GeV/c simulation data sample with 20,000 single $\mu^-$ , $\pi^-$ and $e^-$ events. Percentage of secondaries regarding the total amount of particles in the data sample. No restricted pseudorapidity range, as this makes a differentiation of primary and secondary particles impossible. The number of secondary particles with an $\eta$ covered by the SCT barrel is significantly lower. Only photons with $p_t > 1$ MeV/c are listed. . . . .	36
4.1	Minimal required transverse momentum required for a particle to reach a specific layer of the SCT. . . . .	45
6.1	Comparison of the hit rejection rate of hits in percent for cluster size cuts ( $> 2$ ) and offset cuts (10 GeV/c) with or without edge recovery, applied to 50 GeV/c and 0.2 GeV/c muons. Two data sets were used: full data and a selection of events with only hits from primary particles. Short strip layers only. . . . .	59
6.2	Comparison of the hit rejection rates of hits in percent for different particles. The cluster size cuts (cluster size $> 2$ ) and offset cuts ( $p_t < 10$ GeV/c) were applied to $p_t = 50$ GeV/c and $p_t = 0.2$ GeV/c single particle events. These values include hits from secondary particles. Short strip layers only. . . . .	61
6.3	Hit rejection rates of hits in single muon events in percent, for different orders of application in a subsequent application of the cuts: offset cut applied before cluster size cut ( $os \rightarrow cs$ ) or vice versa. Comparison of the combined application with individual application. Thresholds: cluster size $> 2$ , offset: $p_t > 10$ GeV/c. Short strip layers only. . . . .	61
6.4	Percentage of the events containing at least one track with a reconstructed $p_t > 10$ GeV/c. . . . .	67



## B Bibliography

- [1] A. Abdesselam, “High Luminosity Upgrade.”,  
*<http://atlas.web.cern.ch/Atlas/GROUPS/UPGRADES/>* (May 2011)
- [2] ATLAS Collaboration, “ATLAS Detector and Physics Performance - Technical Design Report”, CERN/LHCC 99-14, 1999
- [3] ATLAS Collaboration, “The ATLAS Experiment at the CERN Large Hadron Collider”, JINST vol. 3, no. S08003, 2008
- [4] ATLAS Run Queries *<http://atlas-runquery.cern.ch/>*, (June 2011)
- [5] ATLAS Collaboration, “The ATLAS Simulation Infrastructure”, The European Physical Journal C - Particles and Fields Volume 70, Number 3, 823-874, 2010
- [6] The ATLAS Experiment Homepage *<http://atlas.ch/>* (July 2011)
- [7] ATLAS TWiki *<https://twiki.cern.ch/twiki/bin/viewauth/Atlas/UpgradeDetectorGeometryVersions>*, (May 2011)
- [8] Athena ATLAS Simulation Framework  
*<http://atlas-computing.web.cern.ch/atlas-computing/packages/athenaCore/athenaCore.php>* (July 2011)
- [9] CERN - European Organization for Nuclear Research - Public Homepage  
*<http://public.web.cern.ch>* (May 2011)
- [10] Geant4 Simulation Platform  
*<http://geant4.cern.ch/>* (July 2011)
- [11] N. Konstantinidis, “ATLAS L1 track trigger for super-LHC”, Proceedings of Science, 2010
- [12] Pavel Reznicek, “Tests of semiconductor microstrip detectors of ATLAS detector”, Diploma Thesis, Charles University in Prague - Faculty of Mathematics and Physics, 2003
- [13] S. Schmitt and A. Schöning, “A Fast Track Trigger for ATLAS at Super-LHC”, JINST vol. 5, no. C07013, 2010
- [14] Sven Pirner, “Intelligent Filtering Algorithms for an upgraded Inner Tracker at ATLAS”, Bachelor Thesis, Physikalisches Institut der Universität Heidelberg, 2010

- [15] V. Karimäki, “Effective circle fitting for particle trajectories”, Nuclear Instruments and Methods in Physics Research A305 187-191, 1991

Erklärung:

Ich versichere, dass ich diese Arbeit selbstständig verfasst habe und keine anderen als die angegebenen Quellen und Hilfsmittel benutzt habe.

Heidelberg, den (Datum) .....